GROWTH AND INVESTIGATION OF THE SLATER-PAULING BEHAVIOR BY X-RAY CHARACTERIZATION OF SINGLE CRYSTAL BCC Fe_x-Mn_{1-x} THIN FILMS ON MgO(001)

by

Harshawardhan Ramesh Bhatkar

A dissertation submitted in partial fulfillment
of the requirements for the degree

of

Doctor of Philosophy

in

Physics

MONTANA STATE UNIVERSITY
Bozeman, Montana

January 2015

To my parents, Mridula and Ramesh
& my life partner, Supriya- for the purpose you brought to my life, for all your support and sacrifices.

ACKNOWLEDGEMENTS

Sometimes, it takes a village to raise a kid. Rightfully, it humbles me when, I have so many people to acknowledge, who have educated me in aspects of research, academics, leadership and life. The first person, to whom I extend my most sincere gratitude, is my advisor Dr. Yves Idzerda. I have learnt from him how to carry out research and I have strived to imbibe his leadership qualities. Apart from financially supporting me; for numerous travels to National Laboratories and conferences, that introduced me to the larger picture of research, his expertise in lab taught a lot more.

My deep gratitude to my lab-mates: Vanessa Pool, Martin Finsterbusch, Alex Lussier, Ezana Negusse, Adam McClure, Hongyan Li and Suzie Flentie for making the lab a friendly place. Only superlatives can attempt to thank Margaret Jarrett. Many thanks to the staff of the Physics Department- Sarah Barutha, Norm Williams, Bo Glaspey, Jeremy Gay and Jodie Hirsch for streamlining related work with element of fun. I am particularly grateful to Dr. Charles Kankelborg and Dr. Paul Rugheimer for sharing their wisdom on life, encouraging and listening to me through my hard times.

The hardships of living in a different country could only be forgotten due to friends who were like family- thanks Masha Kazachenko, Jacob, Vincent, Carlina, Silvina and my roommates. Many thanks to Office of International Programs- Debra Debode, Nathalie Caillaud, Deborah Chiolero for their constant encouragement.

I acknowledge everyone who, though not mentioned here, has made this endeavor exciting and enlightening.

TABLE OF CONTENTS

TABLE OF CONTENTS CONTINUED

LIST OF FIGURES

Figure Page

LIST OF FIGURES CONTINUED

Figure Page

ACRONYMS

AFM	Anti Ferromagnetism / Anti Ferromagnetic
AMR	Anomalous Magnetoresistance
bcc	body centered cubic
DM	Dzyaloshinskii-Moriya
EB	Exchange Bias
fcc	face centered cubic
FM	Ferromagnetism / Ferromagnetic
GMR	Giant Magnetoresistance
MBE	Molecular Beam Epitaxy
MgO	Magnesium Oxide
MR	Magnetoresistance
SV	Spin Valve
TMR	Tunneling Magnetoresistance
QMS	Quadrupole Mass Spectrometer
XAS	X-ray Absorption Spectroscopy
XMCD	X-ray Magnetic Circular Dichroism

ABSTRACT

Magnetic memory storage industry is always searching for materials that can store, read, and write data ever so faster, with lower power, with accuracy and on denser packaging. The material research was spurred with discovery and successful implementation of Giant Magnetoresistance phenomena into critical components of devices. GMR devices essentially were multilayered thin films of a set of magnetically ordered metals. Fe-Mn thin films were used to create one of its moment pinning layers. Fcc Fe-Mn thin films were studied enthusiastically for their AFM properties but very little was known about the rare bcc structured single crystals. Bcc Fe-Mn was found to be ferromagnetic in parts of phase diagram of Fe-Mn.

The magnetic moment of alloys usually follows a regular linear trend based upon electronic configuration of constituent elements, known as Slater-Pauling curve. While most alloys follow the trend, bcc Fe-Mn binary alloys show a dramatic collapse in the bulk magnetic moment, as concentration of Mn is varied.

In this work, we successfully fabricate bcc single crystal thin film of Fe-Mn on MgO(001) substrate by Molecular Beam Epitaxy method. We confirm using Reflection High Energy Electron Diffraction that, the bcc phase of Fe-Mn thin film is achieved, albeit being a forced structure, stable up to 35% of Mn concentration. X-ray absorption spectra of individual elements were used to confirm the compositions of Fe-Mn films and x-ray magnetic circular dichroism was used to track the elemental magnetic moment as the composition was varied. We found that the magnetic moment of Fe drops faster than expected and Mn has very small identical moment in all compositions. We also successfully created a compositionally graded Fe-Mn sample in MBE and spatially mapped its Fe moment by around the critical composition.

The mechanism for collapse of magnetic moment over a spread of composition of Mn is a very complex problem yet we provide our experimental findings of unprecedented resolution to confirm that bcc Fe-Mn can be structurally stable up to 35% Mn and that the magnetic moment of the alloy starts with onset of Fe moment at 14% Mn and is complete by 17% Mn.

CHAPTER ONE

INTRODUCTION TO DISSERTATION

The primary goal of this work is to investigate the peculiar feature in the Slater Pauling curve of Fe-Mn binary alloy thin films. The Slater Pauling curve summarizes a trend in the magnetic moment of transition metal alloys with respect to the atomic number[1, 2]. Fe-Mn alloy follows the trend only for very small concentrations of Mn as a dilution[3]. The question arises, at what concentrations of Mn, does the magnetic moment collapse in the body centered cubic (bcc) thin films and is it different than the bulk? Also, can we track the elemental magnetic moments of the alloy as we vary the concentrations? Tracking of the elemental moments could help the theorists in choosing right modeling that would describe the behavior of larger set of alloys. Though the face centered cubic (fcc) structure of Fe-Mn alloy thin films is studied as an 'exchange bias' (EB) material and employed in industrial applications widely[4], much less work has been reported on bcc structure of Fe-Mn. To answer these questions, challenging task of stabilizing the bcc structure and accessing the elemental moments of this complex system had to be achieved.

First, I was to make high quality single crystal thin films of increasing concentration of Mn in Fe to ensure the presence of, and if possible extend, the bcc structure in the phase diagram of Fe-Mn into regions not accessed in the bulk. To achieve this, I started to work on Molecular Beam Epitaxy (MBE) system. I had to pick up the

technique and available instrumentation to make the films that were reported by only one research group any literature so far.

Second step was to understand the X-ray absorption spectroscopy (XAS) technique and its details to track the element specific information. I got to learn a new capability at the Advanced Light Source, that of 'Fast Scans', which shortened the time required to take the data by 10 fold. This enabled us to use that speed to rapidly take data to make a map of XAS information on a two dimensional grid of the sample. I had opportunity to visit the synchrotron at Berkeley multiple times in the course of the work and it has opened up a new field of interest for my future work.

The work can be extended into more combinations of binary or ternary systems which could be of interest as exchange bias materials for applications in memory devices. One such binary system of interest is Co-Mn, has already been made in the MBE system. Though the primary results are being analyzed, the MBE system can be used to make more such materials. The analysis of data acquired in the XAS mapping can be huge and one needs to work on a computer code that can generate the maps from the data without human oversight.

Historically, the memory in storage devices of computers was essentially a series of aligned or anti-aligned magnets. The way the memory was coded; was in terms of direction of the domains of tiny grains of magnetic material. The physical size of the entire memory storage device was a direct consequence of how small and densely packed could these tiny magnetic particles be packaged. The bits- as they are referred to- became smaller and it was important to detect and manipulate these tinier structures for

reading and writing the memory. To do so effectively, due to enhanced understanding of exchange bias, a new technique involving multilayered metallic sensors were invented for the read and write heads. The Giant Magnetoresistance (GMR) was employed to the read heads. The change in the science and technology was extremely dramatic and the scientists won 2007 Noble prize for Physics.[5] The GMR effect is achieved in a special multilayered nano or micro scale structure. In this structure, the current is drastically sensitive to the charge and spins of the electrons. Such a device is made up of two ferromagnetic electrodes whose relative magnetization orientations can be switched between parallel and antiparallel configurations. For maximal GMR effect to occur of one of the layers is AFM which acts as a pinning layer over which a soft magnetic layer is deposited. These multilayered devices are called Spin Valves (SV). The SV elements are at the core of the read write heads of current magnetic storage packages. (see Figure 1-1)

The Fe-Mn thin films have demonstrated their usage in the modern computer memory devices. The need for faster switching, low power memory technology has propelled the research community to go in search of materials which can outperform the state of the art in-production devices. Fe-Mn since then has been replaced by some other materials such as Ni-Mn or Pt-Mn, Ir-Mn for their engineering properties. [6, 7]

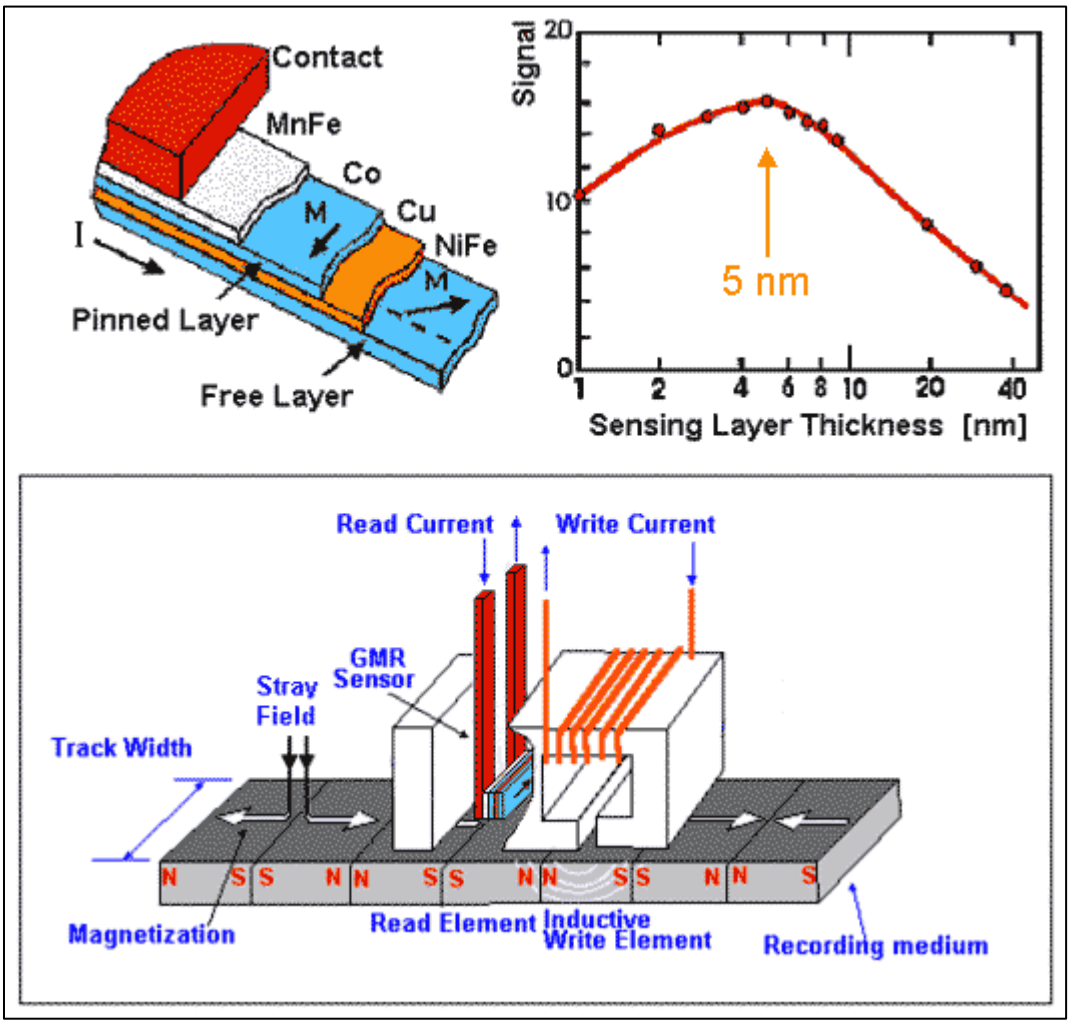

Figure 1-1 GMR read write head for modern hard-drive. Figure from http://www.chem.wisc.edu/, Course 801. 2000.

Overview of Dissertation

Our goal is to investigate the peculiar Slater-Pauling behavior of bcc Fe-Mn thin film. The problem is described in the previous section and has been mentioned in introduction of manuscript chapters later. In order to perform experiments, I used Molecular Beam Epitaxy as growth. The nuances of our growth method are described in the section of MBE in Chapter two (Fabrication) and also in the experimental sections of the manuscripts.

In Chapter three (Analysis), I have explained the concept of X-ray absorption spectroscopy with some labor. This chapter is an attempt to pen down most of the necessary details about XAS and synchrotrons. In following sections a brief discussion explains our use of other experimental techniques, namely RHEED and RBS.

Chapter four describes in detail the successful fabrication of bcc Fe-Mn films and elemental magnetic moment data. Chapter five has details of the moment mapping experiment. In the final chapter (6), I summarize the work discussing a possible model for explanation of the behavior of magnetic moment for Fe-Mn alloys made in this work.

References

1. Slater, J.C., Electronic structure of alloys. Journal of Applied Physics, 1937. 8(6): p. 385-390.

2. Pauling, L., The Nature of the Interatomic Forces in Metals. Physical Review, 1938. 54(11): p. 899-904.

3. Bozorth, R.M., Atomic Moments of Ferromagnetic Alloys. Physical Review, 1950. 79(5): p. 887-887.

4. Nogues and I.K. Schuller, Exchange bias. Journal of magnetism and magnetic materials, 1999. 192(2): p. 203-232.

5. Berkowitz, A.E. and K. Takano, Exchange anisotropy - a review. Journal of Magnetism and Magnetic Materials, 1999. 200(1-3): p. 552-570.

6. Yuasa, H., et al., Method for manufacturing a magneto-resistance effect element and magnetic recording and reproducing apparatus. 2012, Google Patents.

7. Yuasa, H., et al., Method for manufacturing a magneto-resistance effect element and magnetic recording and reproducing apparatus. 2012, Google Patents.

CHAPTER TWO

FABRICATION OF SAMPLES

Molecular Beam Epitaxy (MBE)

To reduce the complexity that may be introduced due to imperfections in structure of thin films, there is need for extremely controlled growth of material. To achieve this, ultra high pure material is deposited in ultra-high vacuum using evaporation techniques. Molecular beam epitaxy is most suited for pure metallic thin film deposition. The word Epitaxy entails growth of the top layer of material in registry with the underlying layer of substrate. Atoms which arrive at the surface of the substrate in the form of a beam, can hop around to settle themselves according to local potential wells and energetics. These atoms are called ad-atoms. The result is an ordered single crystal usually of the same structure of the surface layer of the substrate immediately under the deposited material.

The growth of high quality single crystal films is very sensitive to vacuum conditions, growth temperature, evaporation rates, substrate temperature and chemical-mechanical compatibility of substrate with deposited material. The vacuum conditions play a very important role in determining inter-coupled growth parameters such as evaporation rates, crystallinity of the film and substrate temperatures. The goal is to create very high purity metallic films which are of simple crystal structure like bcc in our case, which are single crystals, which are grown at a rate suitably fast enough such that least amounts of growth defects are trapped and are atomically grown.

Ultra-high vacuum (pressure less than 10^{-9}Torr) in the chamber and possible cold walls of the chamber make the contaminant gas density so low that the mean free path of the atomic (molecular) beam is of the order of 10,000 meters. This means, each atom in the atomic beam will have a collision with a contaminant gas molecules on average only once in 10 kilometers! The size of our chamber is of the order of 1 meter^3, this means that once the atoms of metallic source leave the evaporation vessel, they practically do not collide with anything, until they hit the substrate in a line-of-sight trajectory. This ensures 'beam' nature of the deposition material and very high purity of the films. More details can be found in many books on MBE. [1]

The growth rate also determines the amount of contaminants or defects in a peculiar way. Depending on the UHV conditions, the total number of contaminants striking the substrate is directly proportional to the time taken for completion of the next layer of the deposition material. In other words, slower growth may favor thermodynamic stability but could still allow too many contaminants to settle on the surface, reducing quality of the film. Also, too fast of growth will result in incomplete re-arrangements of atoms as new material will arrive before the previous atomic layer has settled into best positions. This will result in high number of trapped defects and thus inferior crystallinity in the final film.

The nuances of growth on the deposition material over the substrate are determined by the surface chemistry and thermodynamics at the interface. The hopping of ad-atoms is facilitated by higher thermal energy at the surface, but too much heat can affect the adhesion of the material to the surface consequentially creating ball like

growth. If the temperature of the surface of substrate is lower than optimum, then the atomic layers form with defects that could not be filled in by hopping of ad-atoms into those places. So again, the crystallinity suffers, if the temperature of the substrate is incorrect. Surface chemistry is altered, if there are chemically active contaminants already present on the substrate. Thus chemical cleaning of the top surface of the substrate is very critical and usually is a prescribed process for various types of substrates. This process is explained in a later chapter. The fluxes were measured by a UTI instruments, Quadrupole Mass Spectrometer (QMS).

It is natural to assume that, the source materials should be as pure as mentioned on the original purchased commercial packaging. Yet, it was found in earlier work in the group that, further cleaning of some sources was beneficial to avoid any carbon deposition from the sources. When source material is stored in industrial grade plastic bottles or transported in polymer bags, there is a chance that the metal pellets or chunks, which guarantee better than 99.99% purity within the solid mass, have collected organic deposits on the outside. This creates a carbon repository that floats in the Knudsen evaporation cell upon first heating. Thus I have also found that, first few growths after changing the evaporation sources do not produce very high quality films and are possibly contaminated with carbon and also with oxide layer that gets emitted along with the pure atomic beam. As the MBE system is run for long time, the evaporation cells stabilize their emission rates, evaporated material acting also as ‘getter’ of contaminant gasses in the chamber, improves the vacuum base pressure of the chamber.

Evaporation cells or Knudsen cells operate at high temperatures and are shielded from the chamber by chilled water cooled cryo-shrouds to maintain UHV conditions. The Iron source was chosen to be at 1400 °C, as the deposition rate of iron at that temperature was calibrated also in previous work using Rutherford Back Scattering method. The calibrated rate of deposition of Iron at 1400 °C was about 2.5(+-.2) nm/min. With Mn rates factored in, the total deposition of Fe-Mn films was about 20nm in 60 minutes.

The shutters built over the Knudsen cells stop the beam from reaching the substrate. The operation time of the shutter even though operated manually, is fast enough to create atomically abrupt layers. One way to reduce concentration of Mn was to open and close Mn shutter every minute of growth at particular temperature. This effectively gives 50% less Mn at the same temperature of Mn Knudsen cell.

Sample Preparation

Single crystal MgO (001) substrates were bought commercially. For making single film samples of high crystallinity, the substrates were cleaned before being loaded into vacuum chamber. To remove any organic adsorbates and oxides the substrates were heat treated to 800°C to flash clean the top surface in high vacuum. The method is routine for depositing Fe films on MgO substrates. A representative diagram of the growth is in Figure 2-1. Gradient sample was achieved by offsetting the flux lobes (keeping substrate in an off-centered location).

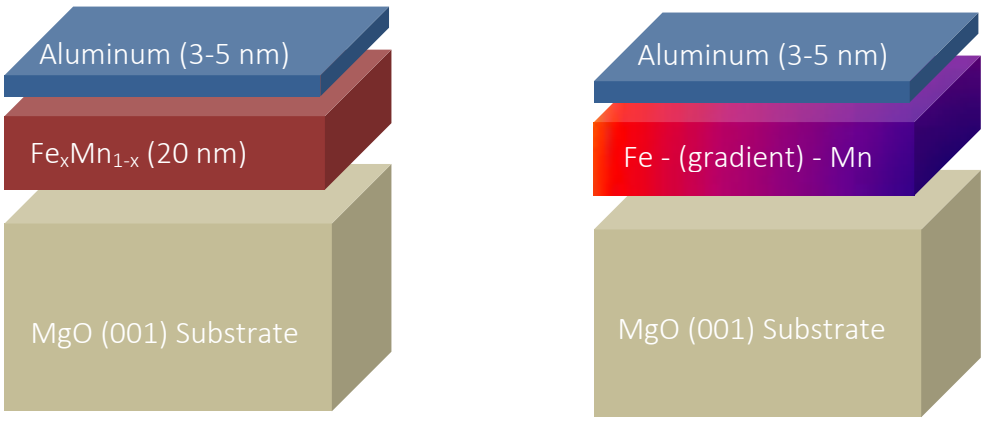

Figure 2-1 Left: FeMn single composition film on MgO (001) substrate with Aluminum capping to prevent oxidation. Right: Offset position created a sample with composition gradient used for mapping

References

1. Herman, M.A. and H. Sitter, *Molecular beam epitaxy : fundamentals and current status*. Springer series in materials science. 1989, Berlin ; New York: Springer-Verlag. xii, 382 p.

2. Jonker, B.T., G.A. Prinz, and Y.U. Idzerda, *Interface Formation and Film Morphology for Growth of Fe and Co on Znse(001).* Journal of Vacuum Science & Technology B, 1991. **9**(4): p. 2437-2444.

3. Prinz, G.A. and J.J. Krebs, Molecular-Beam Epitaxial-Growth of Single-Crystal Fe Films on Gaas. Applied Physics Letters, 1981. 39(5): p. 397-399

CHAPTER THREE

ANALYSIS TECHNIQUES

Reflection High Energy Electron Diffraction

RHEED is a surface sensitive, surface characterization technique used in Molecular beam epitaxy deposition systems while the growth is in progress. The surface quality of epitaxial growth is qualified by RHEED as the surface is being deposited by material. The presence, quality and the locations of the features in the RHEED image gives information about the crystal-quality and some quantitative measurements.

The setup involves an electron gun and a fluorescent screen at very shallow grazing angle on either sides of the sample. Such low glancing angle makes the incident electrons interact with very limited depth of the sample, mostly just the top few layers of atoms. The electrons are accelerated in the gun to energies about few Kilo-Volts, this tunes the wavelength of the electrons close to the lattice spacing of the crystal of the sample. These waves are thus diffracted by the regular pattern of the atomic arrays on the surface of the sample and that results in a pattern of bright spots or lines on the fluorescent screen on the opposite side of the gun.

By orienting sample in specific crystallographic position we can confirm which structure we are seeing at the surface and as we rotate the sample, patterns corresponding to other orientations can be seen emerging on the phosphor screen.

Setup diagram:

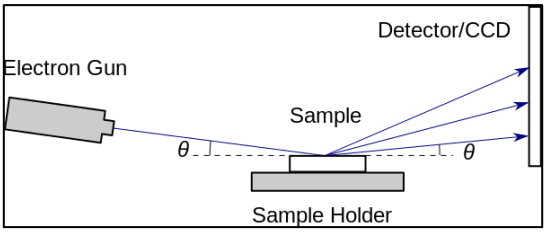

Figure 3-1-1 RHEED setup

RHEED of MgO

The surface quality of the pure surface of MgO substrate was a crucial step in achieving single crystal films of Fe and Mn. The cleaning process of the substrate mentioned later made certain that, the surface of MgO was pristine and had good quality for the epitaxial growth.

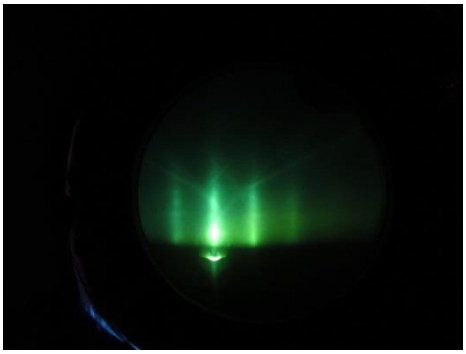

Figure 3-1-2 RHEED Image of MgO crystal showing streaky nature and Kikuchi lines due to terraced nature of surface

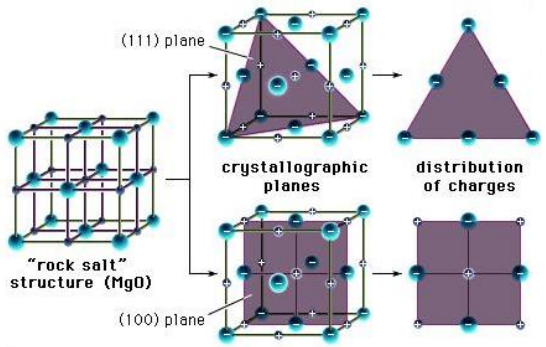

Figure 3-1-3 MgO Single Crystal Structure (Figure from britannica.com)

The MgO crystal lattice structure is essentially a cubic "rock salt" structure. The 001 plane being low index plane is very stable and has square arrangements of Mg and Oxygen atoms seen from top. See Figure 3-1-3.

RHEED of Fe

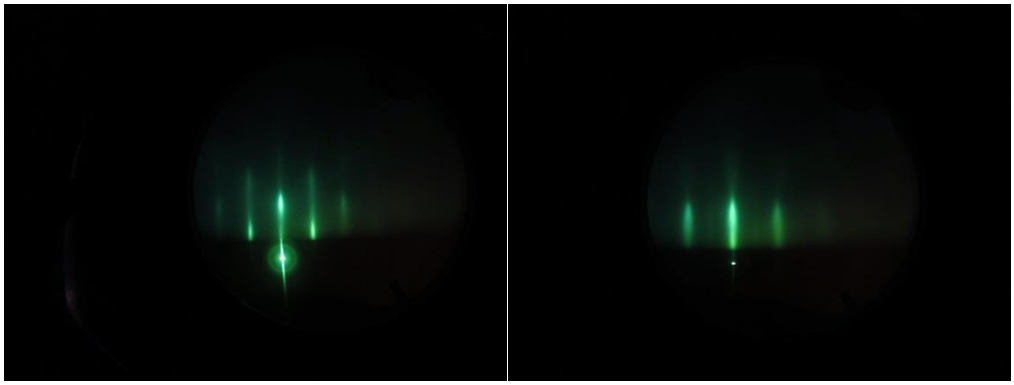

Figure 3-1-4 RHEED images of two orientations of Fe on MgO

As established by the manufacture's specifications, square lattice constant ($a_{MgO<001>}$) of MgO is 4.216Å. For Fe <001> plane, $a_{Fe<001>}$ is 4.06Å. The Lattice constant of Fe<110> is 2.867 Å. The square lattice of Fe<001> rotates by 45° and settles on MgO<001> so that the mismatch between layers minimizes the bi-axial strain. The

difference is only 3.7% after rotation. This kind of epitaxial growth is called "psuedomorphic" growth. A visual is given in Figure 3-1-5.

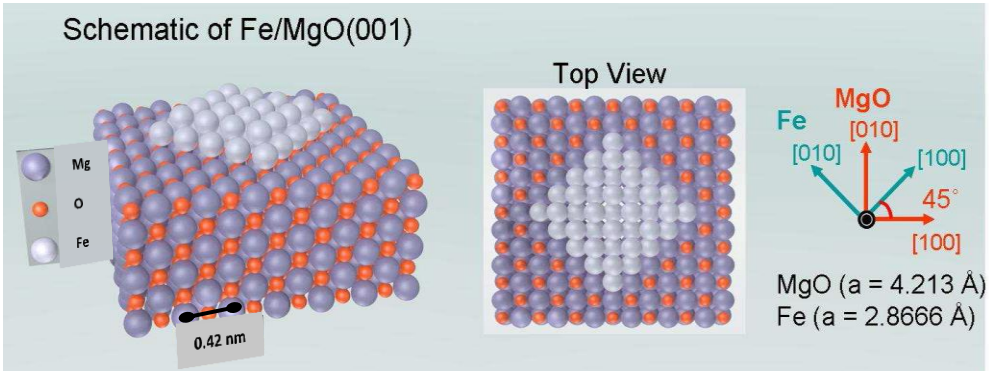

Figure 3-1-5 Schematic of psuedomorphic growth of Fe on MgO(001) [Diagram adapted from Jookyung Lee, Ph.D. Thesis 2010]

X-ray Characterization Methods

All the samples that were grown at the Montana State University were taken to Advanced Light Source at the Lawrence Berkeley National Laboratory, Berkeley, California for x-ray spectroscopic measurements. This chapter gives an overview of what is synchrotron radiation source, how do we get x-rays that can be tuned to a specific energy range and selected polarization to perform all the experiments done in this work. In this section, I will discuss x-ray spectroscopic techniques that have been used for research. Some techniques have been listed for the sake of completeness of the overview.

Synchrotron Radiation Source

When charged particles travel in curved paths they emit radiation, this is synchrotron radiation in one sentence. In these massive facilities, the charge particles

usually are electrons generated by electron guns which are accelerated by Linear Accelerator. These accelerated electrons then enter Booster ring which increases their energy to final energy by radio-frequency electric field that is synchronized with electron trajectory along the curved vacuum tube. These electrons with their energies now about 1.9 GeV are kept in a confined path inside the Storage ring using dipole magnets along with quadrupole and sextupole magnets to focus and to correct for any aberrations in the trajectory.

Bending magnets are used to make the electrons turn from their straight path causing a brilliant sweep of emitted radiation in a tight cone. The narrow focused searchlight like shape of this radiation is due to relativistic effects on the observed pattern of electrons travelling at 99.999996% of speed of light. These tight cones of radiation are sent into long straight tubes what are called beamlines, where various kinds of experiments can be setup. Seen below in Figure 3-2-1.

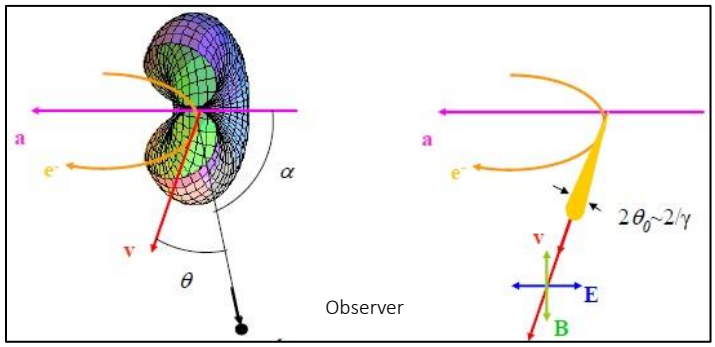

Figure 3-2 -1 Radiation pattern of accelerated electron, in rest frame of charge (left) and in frame of observer (right) Radiation comes out in a tight cone. (Figure adapted from Ref book: Stohr)

To select certain energy from a very broad spectrum synchrotron radiation, the beamline we used for this work, namely Beamline 6.3.1 has a set of grazing angle x-ray grating monochromator with 4 different grating elements. Monochromator basically is a diffraction grating which splits the incoming multi-wavelength beam of light into spatially resolved spectrum. Thus by selecting the angle of incidence over the grating, we can send a narrow range of wavelengths (or energies) through the exit slits onto our sample. By continuously varying the angle of the optics, we can continuously change the energy of photons incident on the sample. Such a synchronized motion of X-ray grating, focusing mirrors and accurate timing of measurement events has been used to make a very rapid scanning technique at Beamline 6.3.2, called the fast scan.

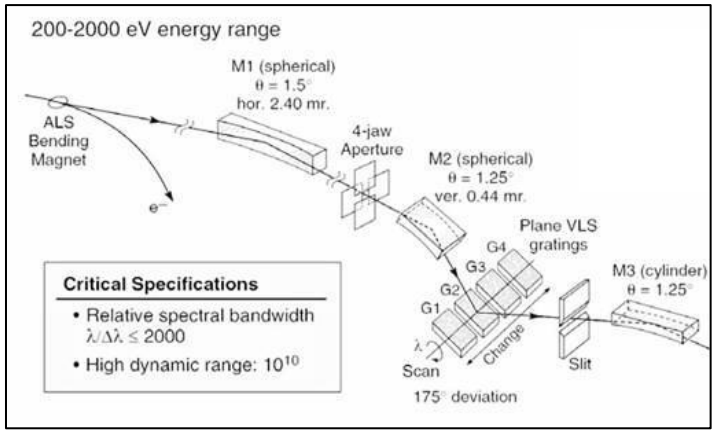

Figure 3-2-2 Beamline 6.3.1 schematic plan (from Beamline webpage)

To select polarization of the x-ray beam, the beam is taken either from above or below the plane of the trajectory. Owing to the projections of angular momenta, the x-ray beam above and below the plane is noted to be of either Left Handed (LH) or Right

Handed (RH) circularly polarized as shown below. When accelerated electron radiates, the process conserves the energy and momentum of the electron-photon system. Thus for radiation emitted in the plane of the orbit, the x ray propagation direction z is perpendicular to $\boldsymbol{L}$ thus the x-rays have $L_z = 0$, namely Linearly polarized. On the two sides where L_z has finite non-zero projection, the geometry dictates that we get LH above the plane and RH below the plane of the orbit.

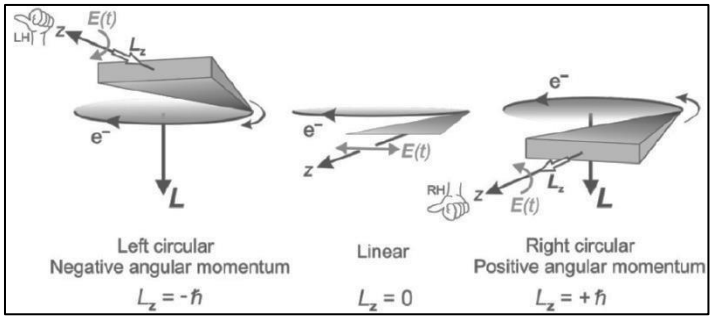

Figure 3-2-3 achieving polarized x-rays in a synchrotron. Left circular, Linear and Right circular polarizations are shown (Figure from Ref. Stohr.)

X-ray Absorption Spectroscopy (XAS)

When light is incident on a material, it gets absorbed and it excites the electrons of the material. The participating electrons hop to higher energy level, if the energy of the incident light matches the difference between initial state and the final state of the electrons. This kind of transition is called resonant absorption. If the electrons participating in such a transition happen to be from the core state rather than the superficial outer states, the energy required to excite them may well be in the soft x-ray region. The x-ray photons then, excite the core level electrons to higher available state which may be either a bound state or a state in free space- causing ionization. As for the

outgoing electron, it creates a vacancy in the core state momentarily. This vacancy may be referred to as a "core hole". Many processes have been shown to exist, by which, a core hole gets filled up again by nearby electrons. Auger process is one such example. The outgoing electron, in such a case, turns out to carry a lot of information about its local environment from where it was ejected. Many interactions between the outgoing electron and its surroundings have been identified so far.

In atoms, transition probability is approximated by what is called as Fermi's golden rule, shown below,

$$W_{fi} \propto \sum_{q} \left|\langle \varphi_f | \boldsymbol{e_q}.\boldsymbol{r} | \varphi_i \rangle\right|^2 \delta\left(E_f - E_i - \hbar\Omega\right)$$

Where
φ_f = final state
φ_i = initial state
$\boldsymbol{e_q}.\boldsymbol{r}$ = dipole radiation operator
$E_f - E_i$ = energy difference between final state and initial state of atomic electron
$\hbar\Omega$ = energy of incident photon (x-ray)

This describes one atomic interaction. One can realize that in a solid, depending upon the constituent elements, for certain energies there will be a sharp rise in the number of such transitions. This creates the sharp rise in the intensity of absorption of x-rays.

The energy, at the absorption edge, where most of the electrons in the solid start to make the transition, marks the minimum energy difference between the Fermi level and the core state- namely the binding energy. Binding energies for various core electrons in various elements are unique and characteristic to the transitions. Using the database available for the entire periodic table, each absorption edge can be identified to a specific

transition of a specific element. The elemental absorption edges that are used in current study are called L_3 and L_2 edges. (See Figures 3-3-1, 3-3-2) The transitions that are from $2p_{3/2}$ core level of element to an empty 3d state near Fermi level are labeled as L_3 edge and those from $2p_{1/2}$ to 3d are labeled as L_2 edge.

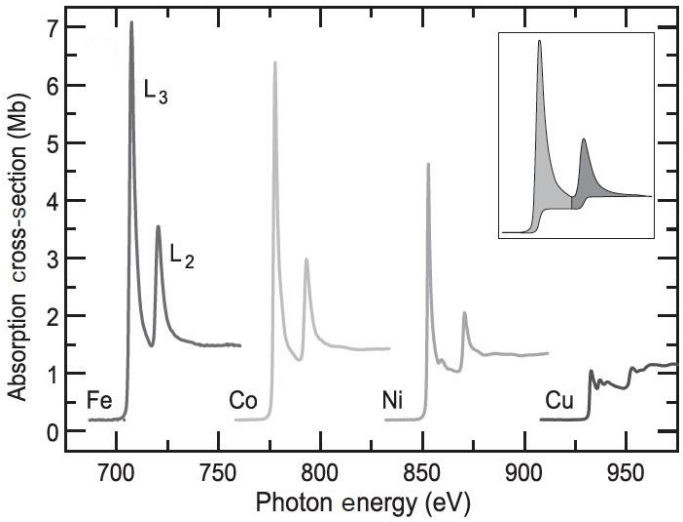

Figure 3-3-1 "L edge" X-ray absorption cross section of transition metals plotted vs. photon energy. Shaded inset shows contribution of area under the curve used to indicate sum of L intensities. Fe has highest area and Cu has least total area.(Fig. from Ref: Stohr)

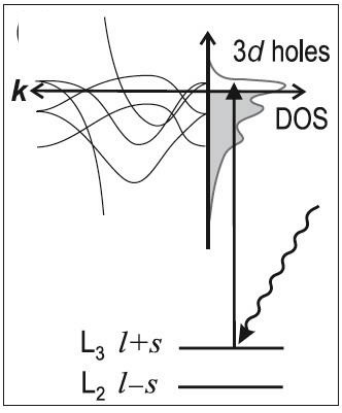

Figure 3-3-2 Simple density of states picture of XAS process illustrating origin of two L edge transitions. (Fig. from Ref: Stohr)

As an example of pure Fe x-ray absorption spectrum see figure (3-3-3).

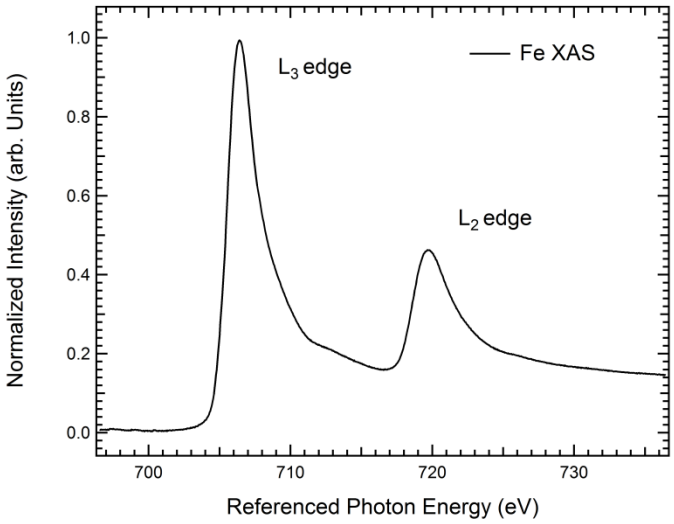

Figure 3-3-3 x-ray absorption L edges of pure metallic Iron thin film

As the relative absorption intensity of the edges depends on the probability of transitions of $2p_{3/2}$ and $2p_{1/2}$, the degeneracy of each of the p state channels results in 2:1 intensity ratio between L_3, L_2 edges.

The x-rays penetrate only a few hundred nanometers into the substrate. The total number of electrons that are measured by the technique is the count of those electrons that replenish the successfully escaped electrons. That includes the sum total of electrons being produced and electrons being re-absorbed by competing processes. In total electron yield technique, we count all the electrons that have escaped the sample, by measuring the current needed to keep the sample electrically neutral. If the incident x-ray photon beam is chosen to be at grazing angle then the projected interaction depth varies and the absorption intensity is now proportional to the interacting depth. This means, we can

chose if XAS should be sensitive to the very top layer of the sample or be insensitive to top layer by making incident beam perpendicular to the substrate surface.

If the electronic states in the final state of transition are part of hybridized orbital, or in a part of chemical state such as an oxide, then the density of states will have a rich structure than just pure elemental L edge peaks.

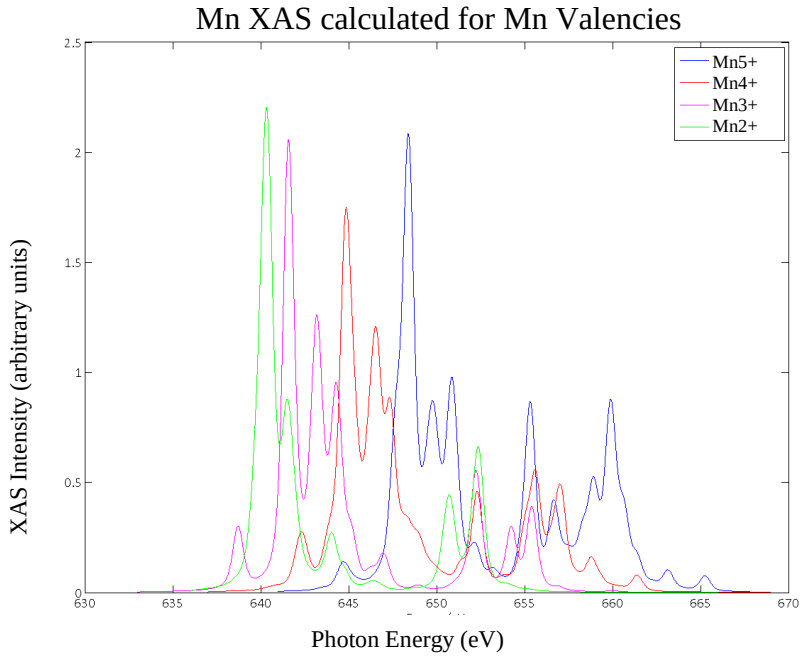

Figure 3-3-4 XAS calculated by CTM4XAS software showing Mn valencies Mn^{2+},Mn^{3+},Mn^{4+},Mn^{5+}. Energy referenced to Fermi energy at 0 Kelvin.

In the figure 3-3-4 I have plotted a calculation of XAS spectrum for various valencies of Mn.This was calculated using CTM4XAS software created by F.M.F DeGroot. The position of the peaks shifts as metal loses electrons from the ground state. Next figure 3-3-5 shows Mn spectra taken at Beamline. This is energy referenced to first peak for comparing the features in the L_3 peak.

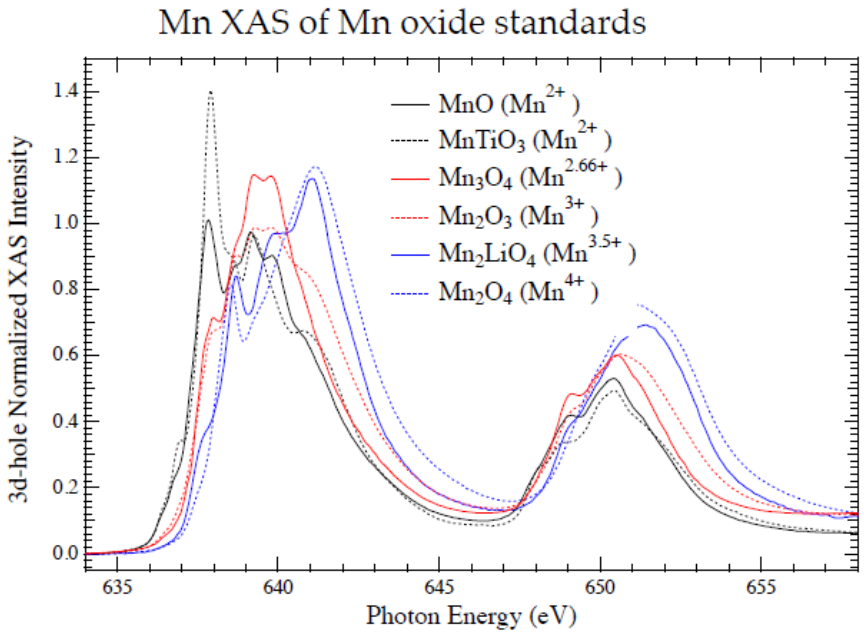

Figure 3-3-5 Experimental XAS showing Mn valencies Mn^{2+},Mn^{3+},Mn^{4+},Mn^{5+}. Energy referenced.

Thus XAS is element specific, surface selective and sensitive to chemical and structural environment non-destructive probe that is used extensively in this work.

X-ray Magnetic Circular Dichroism (XMCD)

The electrons are filled into the shells according to their spin quantum number as explained in the Hund's rules. The electronic band structure probing experiments such as x-ray spectroscopy, interact with electrons using photons. The interactions conserve energy and momentum of the system as expected. The transitions are based on 'selection rules' of quantum mechanics. The spin part of the electronic wave function which carries information about angular momentum interacts with the polarization state of the incident photons. Thus, if the incoming photons are rich in only one type of polarization, only

those electrons can be promoted to excited state, which have the correct spin state according to the selection rules. This means, when polarized x-rays are incident, the states that are usually mapped by regular XAS will be distinguished according to their spin. We get spin resolved information of the states accessed by the XAS experiment. The selection of polarized x-rays is explained in the description of synchrotrons. At the beamline, the experiment is done slightly differently. Rather than moving the entire specialized optics above and below the orbital plane of electrons, the relative orientation of the electronic spin with respect to the polarization direction of the x-rays is set by applying a strong magnetic field to the sample in experiment. This applied magnetic field aligns the majority of the electron spins with its direction. By changing the magnetic field direction by 180°, the two orientations of spins can be exposed to the highly polarized x-ray photon beam. This technique gives us spin resolved density of states just above the Fermi level of the solid and is called X-ray Magnetic Circular Dichroism (XMCD or just MCD).Figure 3-4-1 shows a schematic of XMCD with arrows indicating excitation of particular spin (color) due to interaction with polarized x-ray beam. If the population of two spins is different at Fermi level then the XAS with polarized light will show difference in intensities for two cases. The difference spectrum is XMCD and is depicted in Figure 3-4-2.

The XMCD spectrum is interpreted to be proportional to the magnetic moment of the sample. The population of the unpaired electrons at Fermi level contributes to magnetism. By measuring the asymmetry of absorption and using standards, magnetic moment can be calculated for the samples in the study.

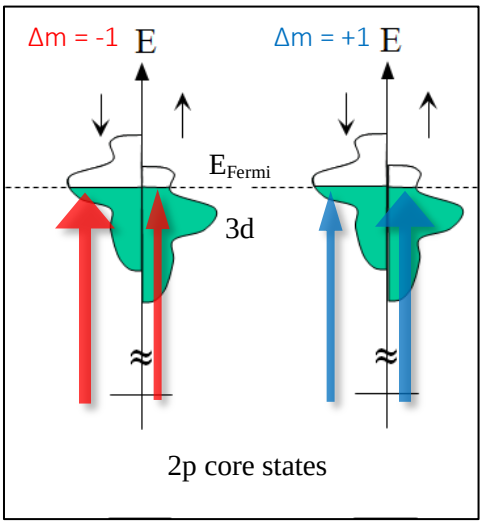

Figure 3-4-1 XMCD illustrated. Majority spin transitions are thick arrows and minority is denoted by thing arrows. Color of arrowd denotes relative x-ray polarization

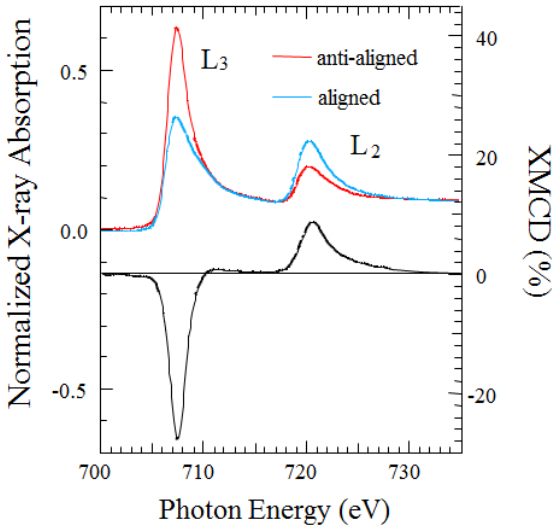

Figure 3-4-2 XMCD of Iron as difference spectrum of spin resolved XAS

Much of the description of the x-ray absorption spectroscopy and synchrotrons can be seen in special books and articles. [1-5]

Rutherford Backscattering Spectrometry (RBS)

The thickness of first few samples was calibrated directly by RBS in Dr. Smith's lab in the department. This method is widely used to find thicknesses of elements which are quite dissimilar in their atomic number. A beam of high energy He ions is incident on the sample and a channeltron counts number of backscattered ions. The number versus energy of backscattered ions is signature of constituent thin film. A program (SIMNRA) helps to create a pseudo model by using parameters of the experiment performed and once fitting is done well, thickness of the layers constituting the film can be read out. In our case, since Fe and Mn are consecutive elements, the RBS failed to clearly establish any stoichiometry. Instead, I used the RBS to calibrate pure elemental growth rates according to the temperature of the sources. This helped to correlate the relative growth rates of Fe and Mn as function of temperature of the ovens.

Note on Errors

The error associated with calculating the concentration gradient comes from temperature readouts, flux rate readouts on QMS and all other instrumental errors associated with XAS measurements. The most significant of this error is in the human reading of quantities such as QMS readouts and temperature, which was minimized by keeping the temperature of growth steady within 1 Kelvin for all growths. The second error that is equally important is the read out of QMS. The readings of flux rates were taken multiple times per growth and error was reduced by taking statistical averages of the relevant quantities. The X-ray measurements were done at various resolutions of

energy, with about 0.1 eV resolution when used with 1200 lines per mm and exit slit of about 20 square microns. The resolution of various instruments was found in their specifications.

References

1. Stavitski, E. and F.M.F. de Groot, The CTM4XAS program for EELS and XAS spectral shape analysis of transition metal L edges. Micron, 2010. 41(7): p. 687-694.

2. Stöhr, J. and H.C. Siegmann, Magnetism : from fundamentals to nanoscale dynamics. Springer series in solid-state sciences,. 2006, Berlin ; New York: Springer. xvii, 820 p.

3. Bunker, G., Introduction to XAFS : a practical guide to X-ray absorption fine structure spectroscopy. 2010, Cambridge, UK ; New York: Cambridge University Press. viii, 260 p.

4. Kittel, C., Introduction to solid state physics. 8th ed. 2005, Hoboken, NJ: Wiley. xix, 680 p.

5. Winick, H., Synchrotron radiation sources : a primer. World Scientific series on synchrotron radiation techniques and applications. 1994, Singapore ; River Edge, N.J.: World Scientific. xix, 507 p.

6. Mayer, M., *SIMNRA, a simulation program for the analysis of NRA, RBS and ERDA.* Application of Accelerators in Research and Industry, Pts 1 and 2, 1999. 475: p. 541-544

CHAPTER FOUR

ELEMENTAL MOMENT VARIATION OF BCC FE_XMN_{1-X} ON MGO(001)

Contribution of Authors and Co-Authors

Manuscript in chapter 4

Author: Harsh Bhatkar

Institution: Department of Physics, Montana State University, Bozeman Montana 59715

Contributions: Made the samples under investigation, collected some XAS data, discussed results wrote the manuscript

Co-Author: Elke Arenholz

Institution: Advanced Light Source, Lawrence Berkeley National Laboratory, Berkeley, California 94720, USA

Contributions: Beamline scientist where XAS data was taken, trained H. Bhatkar for use of beamline also helped in useful discussions

Co-Author: Yves U. Idzerda

Institution: Department of Physics, Montana State University, Bozeman Montana 59715

Contributions: Obtained funding for the project, analyzed x-ray absorption data, edited the manuscript

Additional Contributions: I would also like to acknowledge Adam McClure for critical discussions and training on Molecular Beam Epitaxy system.

Manuscript Information Page

Authors: H. Bhatkar, E. Arenholz, and Y.U. Idzerda

Physical reviews B

Status of Manuscript:

__X_ Prepared for submission to a peer reviewed journal

____ Officially submitted to a peer reviewed journal

____ Accepted by a peer reviewed journal

____ Published in a Peer reviewed journal

The purpose of this manuscript is to provide an introduction to Fe-Mn problem, to explain our motivation to pursue this work and to describe the x-ray absorption spectroscopic data of Fe-Mn films. In this manuscript we describe carefully how the FeMn films were made keeping in mind that BCC structure of Fe-Mn on MgO was not reported before. There is more in-depth discussion on sample preparation describing first structure of Fe on MgO and then how Fe-Mn films were grown using optimized growth conditions.

Abstract

In this paper, we report growth, structural characterization and evolution of electronic structure of epitaxially grown bcc Fe_xMn_{1-x} on MgO(001). Bcc structure of Fe_xMn_{1-x} in bulk materials is seen to be stable only up to x= 0.88. In the thin film form, using the stable structure of Fe on MgO (001), it is observed by electron diffraction, that the Fe_xMn_{1-x} alloy remained bcc much beyond bulk value (x ~ 0.65). The variation in the magnetic moment of bulk Fe_xMn_{1-x} shows accordance to the Slater-Pauling behavior in low x region. But the bulk magnetic moment shows a dramatic collapse near x~0.88. As the elemental moment of Fe in the alloy is investigated by X-ray absorption spectroscopy and X-ray magnetic circular dichroism, we find that even in the 20 nm crystalline bcc films the magnetic moment of Fe abruptly falls between $0.8<x0<0.9$. The elemental magnetic moment of Mn showed no such variation across x.

Introduction

Thin films of fcc Fe_xMn_{1-x} have been of excitement in the area of magnetic storage for considerable time due to their application as the choice alloy in the multilayer systems that form the magnetoresistive read heads [1]. In terms of the exchange-biasing achieved using the Fe_xMn_{1-x} materials, it was observed that the FeMn of 50% concentration was stable in thin film form at room temperature [2], which became the key motivation to study FeMn in various structures and in thin film forms. The antiferromagnetic (AFM) Fe_xMn_{1-x} with various concentrations in fcc phase can be stabilized between 30-50 at% [3] in thin films. Single crystallinity of thin films reduces complexity of the structure in study of FeMn systems. The Fe_xMn_{1-x} single crystalline growth has been stabilized in fcc form with permalloy and on various substrates such as copper [4]. Since the fcc Fe is AFM[5] and bcc Fe is Ferromagnetic (FM)[6], the mechanism of magnetic moment variation becomes interesting in the applications that take advantage of exchange bias of FeMn layer. The bcc Fe-Mn single crystal growth on MgO is reported here. Interface with MgO is of particular interest for TMR devices [7, 8]. Fe-Mn alloys show a sharp deviation from the usual Slater Pauling behavior at low concentration of Mn in Fe-Mn. The magnetic moment per unit atom of Fe-Mn drops from its dilution law and goes extinct at about 15% of Mn in Fe for bulk material. (All percentages are atomic percent.) The Fe-Mn equiatomic alloy is observed to be stable in fcc structure for a large part of phase diagram and shows AFM order. The low concentration of Mn was said to show stable bcc structure only up to 5% in earlier phase diagrams [9] , then later upto 12% [10] and upto 20% on Ga-As substrate [11]. We

observe that high concentration of Mn can be incorporated in Fe in bcc single crystal form on MgO (001) at room temperature by MBE.

The bulk Fe_xMn_{1-x} alloy is intriguing because of its departure from the Slater-Pauling curve. The average moment per atom of nearly all transition metal binary alloys is found to first increase with the number of electrons (alloy composition), then decrease above a critical value. For FeMn, the average alloy moment follows this trend only for the high Fe concentrations (see Fig. 4-1). At ~12% Mn concentration (88% Fe), the bulk average moment rapidly vanishes, suggesting the onset of a magnetic phase transition.

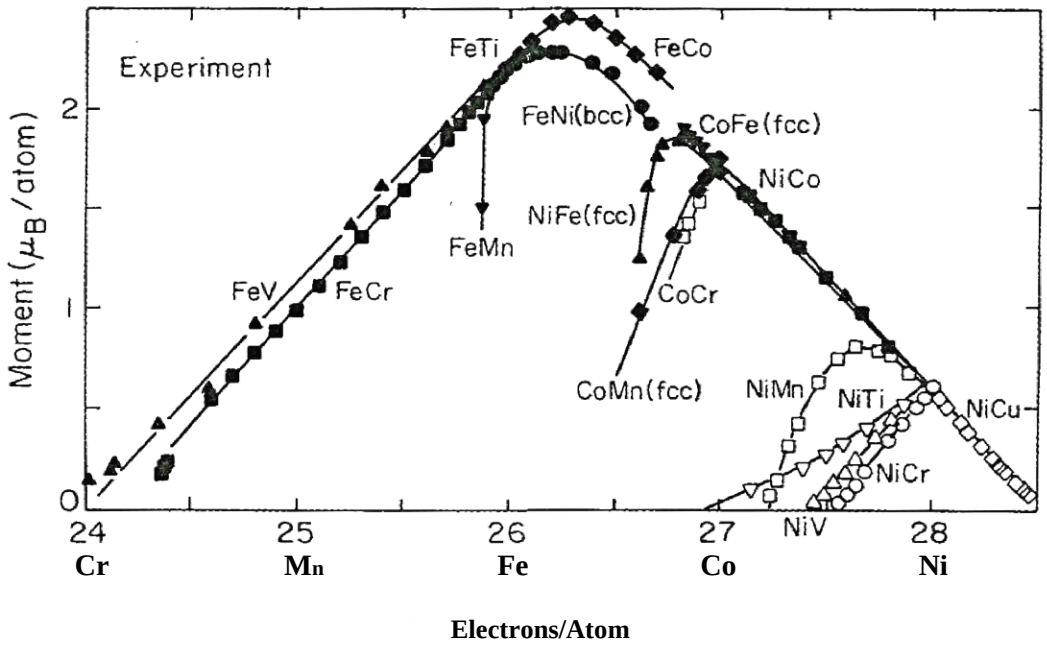

Figure 4-1 Slater-Pauling curve of atomic moment for different transition metal alloys (from Bozorth [12]).

Experimental

Using Molecular Beam Epitaxy, single crystal films of Fe_xMn_{1-x} were deposited on polished single crystal substrates of MgO(001) surface. The MgO substrate cleaning procedure consisted of sonication of the MgO single crystal in acetone followed by sonication in methanol for 5 minutes. Usually, at the third step in the triple wash technique, substrates are washed in de-ionized water, but due to hygroscopic nature of MgO, this final step was deleted. After flowing dry nitrogen over the freshly sonicated MgO, these substrates were quickly mounted onto a molybdenum holder using indium solder and loaded into high vacuum. The substrates were then heat treated to clean any possible adsorbed contaminants by annealing in vacuum at 800 °C (1073 K) for 2 minutes. This cleaning procedure has been shown to produce layer-by-layer growth [13, 14].

The base pressure just prior to growth was ~1.0×10^{-9} Torr and during the growth it raised to ~2.5×10^{-9} Torr with all source Knudsen Cells at their operating temperatures. The Fe source was always maintained at constant temperature of ~1400 °C (1673 K) assuring a constant rate of Fe deposition while the Mn source was held at various temperatures to achieve different alloy stoichiometry for the films. The films were deposited for 60 minutes at 150-160 °C (423-433 K) substrate temperature to ensure good quality, ~20nm thick films [15]. Deposition fluxes were monitored by quadrupole mass spectrometry (QMS). A layer of amorphous aluminum of thickness 3.5-5 nm was deposited as a capping layer. Substrates were cooled to 70 °C (343K) before deposition of the Al capping layer to minimize any interlayer mixing between FeMn film and Al.

The thickness of Al capping layer was limited on the lower bound by depth of the aluminum oxide that forms and on the upper bound, by the probing depth of the photons used in X-ray absorption spectroscopy (XAS). Film compositions were verified by comparison of the Fe and Mn integrated L_3-edge XAS intensities and film thicknesses were calibrated by Rutherford Backscattering Spectrometry (RBS).

Results and Discussion

The bare MgO substrate (001) surface quality was first characterized in ultra-high vacuum environment using *in-situ* Reflection High Energy Electron Diffraction (RHEED) imaging immediately after heat treatment. Since MgO is an insulating material, substrate charging can distort the diffraction pattern, resulting in broad fuzzy lines as seen in the left panel of Figure 2. RHEED was also used to confirm that the growth of Fe_xMn_{1-x} films on MgO (001) is epitaxial and in the bcc phase up to 35% Mn. Representative RHEED images along high symmetry directions of MgO substrate for the Fe_xMn_{1-x} on MgO are shown in the center and right panel of Figure 4-2. The films were of high quality, as indicated by the sharpness and continuous nature of the streaks on the RHEED pattern. Mn concentration beyond 35% showed complex RHEED pattern indicating the loss of bcc epitaxy. Notice that the bcc growth of Fe_xMn_{1-x} films is similar to pure Fe films deposited on MgO where the bcc Fe lattice is rotated 45 degree from the Mn surface net[16]. Thus the (100) direction of the MgO(001) surface coincides with (110) direction of the epitaxial bcc Fe_xMn_{1-x} lattice.

Figure 4-2 RHEED images (LEFT) from the bare MgO(001) substrate taken along the <100> direction, (CENTER) for a 20 nm pure Fe film on MgO(001) along the <100> direction of the MgO substrate, and (RIGHT) for a 20nm $Fe_{80}Mn_{20}$ film on MgO(001) along the <100>

To investigate the elemental moment variation and to examine whether ultrathin films behave similarly to the bulk behavior, 20 nm single crystal Fe_xMn_{1-x} thin film alloys were grown by MBE on MgO(001) substrates and the elemental moments of the Fe and Mn were independently monitored by X-ray absorption spectroscopy (XAS) and X-ray magnetic circular dichroism (MCD). Both were measured in sample current configuration at Beamline 6.3.1 of Advanced Light Source of Lawrence Berkeley National Laboratories. By comparing the integrated L_3-edge XAS individual elemental intensities of Fe and Mn in Fe_xMn_{1-x} one can correlate the Mn source temperature with the concentration of Mn in Fe_xMn_{1-x} films. Precise film alloy compositions could be targeted by control of the Mn flux via the Mn source temperature by using a thermocouple in direct contact with the Mn Knudsen cell crucible. Mn Source temperature was varied from 680°C for the lowest Mn concentration films to 852°C for the highest concentration of Mn in the Fe_xMn_{1-x} films. Figure 4-3 displays the normalized Mn XAS intensity as a function of the Mn temperature, showing the usual trend

explained by August equation The August equation is similar to Antoine equation which describes vapor pressure and temperature relation for pure liquids and gasses.

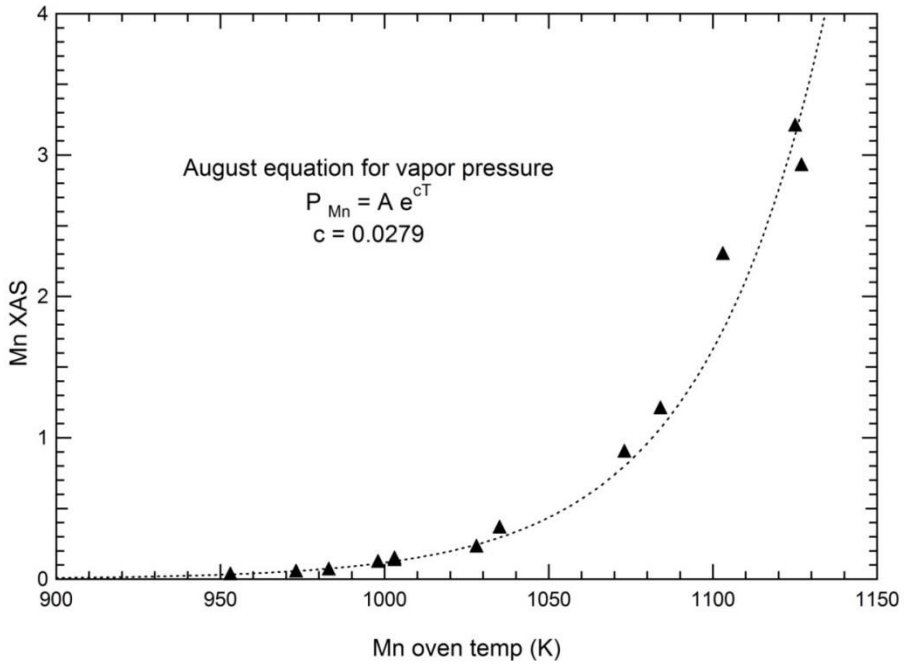

Figure 4-3 Mn XAS intensity vs. Mn oven temperature. The dotted line is a fit to the data using the August equation for vapor pressures, indicating the concentration of Mn incorporated in Fe_xMn_{1-x} as Mn oven temperature increased. The Fe oven temperature was held

Figures 4-4 and 4-5 display the evolution of the peak normalized Fe L_{23}-edge XAS and Mn L_{23}-edge XAS with Mn concentration using linear polarized X-rays, respectively. The energies are calibrated by comparison with reference powders that are measured immediately before or after the Fe_xMn_{1-x} films. The Fe energies are calibrated using a $ZnFe_2O_4$ powder with an L_3-peak energy of 708.22 eV and the Mn energies are calibrated by comparison with a $MnTiO_3$ powder with an L_3-peak energy of 637.90 eV. Additionally, new fast scan capabilities at beamline 6.3.1 minimize the time between

subsequent XAS scans, resulting in more reliable energy values. The Fe L_3-peak energy (Figure 4) shows a small shift to higher binding energy with increasing Mn concentration up to 35% Mn (as shown in the figure inset). Above 35%, where the RHEED images show a change in crystal structure, the L_3-peak energy returns to its original value. The Fe XAS spectra also exhibit an increased broadening in the L_3-peak and a change in the branching ratio (L_3-to-L_2 peak ratio). The Mn L_3-peak energy (Figure 4-5) shows no energy shift with increasing Mn concentration. For the lowest Mn concentrations, the small features at energies beyond the L_2-peak beginning at 651.5 eV are from Mg K-edge absorption features (1303 eV) due to 2nd harmonic light generated by the monochromator.

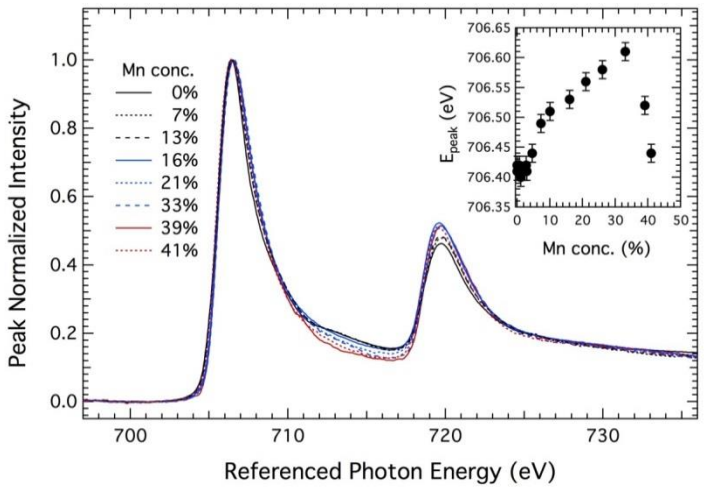

Figure 4-4 Normalized Fe L_{23}-edge XAS spectra for various Mn concentrations. INSET: Fe L_3-peak energy as a function of Mn concentration

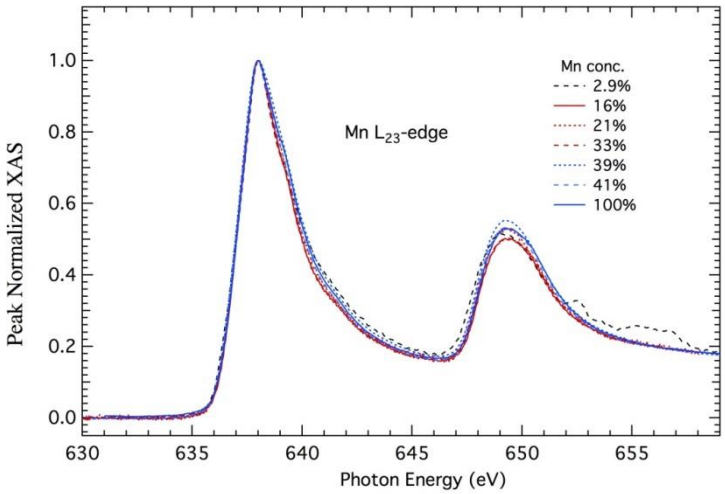

Figure 4-5 Normalized Mn L_{23}-edge XAS spectra for various Mn concentrations.

By using circular polarized light and reversing the magnetization direction at each photon energy through application of a ±500 Oe magnetic field applied along the photon propagation direction, the MCD spectra was measured. After correction for the incident beam direction, incomplete polarization, and variation in perpendicular demagnetization (4□M), the average Fe atomic moment was then determined from the peak of the L_3-edge MCD spectra at each composition for comparison with the bulk behavior as determined by Gumlich (Fig. 7-32 in [17]) and reported in the compilation shown in Figure 4-1. The result (shown in Figure 4-6) shows qualitative agreement between the bulk behavior and the thin film behavior although the thin film moment is present to a slightly higher concentration (15% Mn). It is important to note that the bulk data (open circles) represents the average moment per atom independent of atom type whereas the thin film data (filled triangles) represents the moment per Fe atom, so a direct quantitative

comparison is not appropriate. The thin film data displays a gradual reduction in the average moment with composition followed by an abrupt decrease at x~0.85 which occurs at a slightly higher composition and looks to be much more abrupt than the bulk data reduction. Intriguingly, the Mn shows no robust MCD signal, even at the lowest concentrations suggesting that the net Mn moment is very small, probably due to moment cancelation from spin frustration. This persists even at Mn concentrations as low as 1% and for low temperature depositions (substrate held at RT) to reduce the Mn mobility and prevent Mn clustering.

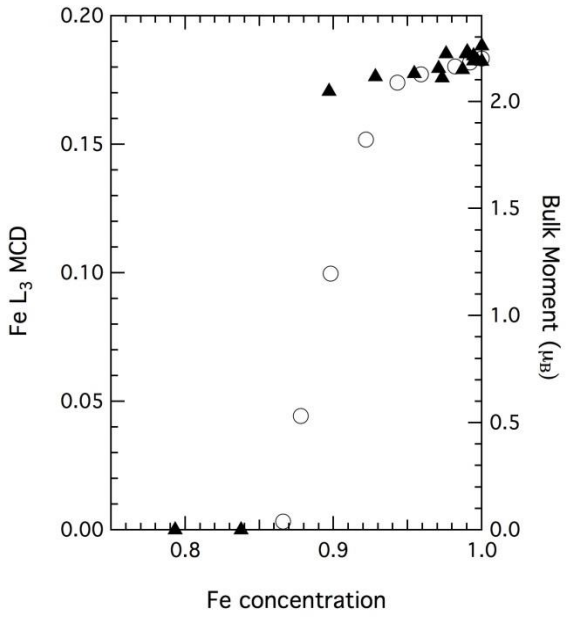

Figure 4-6 Fe L_3-peak MCD as a function of Fe content.(solid triangles) and the bulk average moment (open circles from Gumlich)

Conclusions

The growth of bcc Fe_xMn_{1-x} is psuedomorphic to the MgO (001) surface with a 45° rotation and stable up to x= 0.65 (35% Mn). The elemental magnetic moment of Fe shows a behavior similar to bulk as x is varied from $0<x<0.6$ with a sudden deviation from the linear trend. The elemental moment of Mn in FeMn alloys showed no significant variation.

Acknowledgements

One of us (HB) would like to thank Adam McClure for useful discussions.

References

1. Dieny, B., et al., Giant Magnetoresistance in Soft Ferromagnetic Multilayers. Physical Review B, 1991. 43(1): p. 1297-1300.

2. Hempstead, R.D., S. Krongelb, and D.A. Thompson, Unidirectional Anisotropy in Nickel-Iron Films by Exchange Coupling with Anti-Ferromagnetic Films. Ieee Transactions on Magnetics, 1978. 14(5): p. 521-523.

3. Umebayas.H and Y. Ishikawa, Antiferromagnetism of Gamma Fe-Mn Alloys. Journal of the Physical Society of Japan, 1966. 21(7): p. 1281-&.

4. Tsang, C., N. Heiman, and K. Lee, Exchange Induced Unidirectional Anisotropy at Femn-Ni80fe20 Interfaces. Journal of Applied Physics, 1981. 52(3): p. 2471-2473.

5. Hasegawa, H. and D.G. Pettifor, Microscopic Theory of the Temperature-Pressure Phase-Diagram of Iron. Physical Review Letters, 1983. 50(2): p. 130-133.

6. Park, J.H., et al., Non-collinear magnetism in itinerant electron systems: Fe, Co, and Ni. Journal of the Korean Physical Society, 2000. 37(2): p. 109-113.

7. Yuasa, S., et al., Giant room-temperature magnetoresistance in single-crystal Fe/MgO/Fe magnetic tunnel junctions. Nature Materials, 2004. 3(12): p. 868-871.

8. Parkin, S.S.P., et al., Giant tunnelling magnetoresistance at room temperature with MgO (100) tunnel barriers. Nature Materials, 2004. 3(12): p. 862-867.

9. Hansen, M., Constitution of binary alloys. 2d ed., prepared with the cooperation of Kurt Anderko.. ed. 1958, cNew York: cNew York, McGraw-Hill.

10. Yamauchi, H., et al., MAGNETIZATION OF ALPHA-PHASE FE-MN ALLOYS. Journal of the Physical Society of Japan, 1974. 36(4): p. 971-974.

11. Jing, C., et al., Structure and magnetism of Fe1-xMnx alloys on GaAs (001). Journal of Magnetism and Magnetic Materials, 1999. 198-99: p. 270-272.

12. Bozorth, R.M., Ferromagnetism. 1951, New York: IEEE Press.

13. Koyano, T., et al., The Enhanced Magnetic-Moment and Structural Study of Fe/Mgo Multilayered Films. Journal of Applied Physics, 1988. 64(10): p. 5763-5765.

14. Koyano, T., et al., X-Ray-Diffraction Study of Fe/Mgo Multilayered Films with an Enhanced Magnetization. Journal of Physics-Condensed Matter, 1991. 3(32): p. 5921-5926.

15. McClure, A., E. Arenholz, and Y.U. Idzerda, Ferrimagnetic ordering of single crystal Fe1-xGax thin films. Journal of Vacuum Science & Technology A, 2010. 28(4): p. 969-972.

16. Urano, T. and T. Kanaji, Atomic and Electronic-Structure of Ultrathin Iron Film on Mgo(001) Surface. Journal of the Physical Society of Japan, 1988. 57(10): p. 3403-3410.

17. Gumlich, E., Dependence of magnetic properties, specific resistance and density of Fe alloys on chemical composition and heat treatment. Wiss. Abhandl. Physik-tech. Reichsanstalt. 4: p. 267-410..

CHAPTER FIVE

MOMENT MAPPING OF BCC FE_XMN_{1-X} ALLOY FILMS ON MGO(001)

Contribution of Authors and Co-Authors

Manuscript in chapter 5

Author: Yves U. Idzerda

Institution: Department of Physics, Montana State University, Bozeman Montana 59715

Contributions: Obtained funding for the project, collected and processed the mapping data, wrote the manuscript

Co-Author: Harsh Bhatkar

Institution: Department of Physics, Montana State University, Bozeman Montana 59715

Contributions: Made the samples to be studied, collected some parts of x-ray data, and discussed results

Co-Author: Elke Arenholz

Institution: Advanced Light Source, Lawrence Berkeley National Laboratory, Berkeley, California 94720, USA

Contributions: prepared the beamline facility, helpful discussions

Manuscript Information Page

Authors: Y.U. Idzerda, H. Bhatkar, and E. Arenholz,

Journal Name: Journal of Applied Physics

Status of Manuscript:

_____ Prepared for submission to a peer reviewed journal

_____ Officially submitted to a peer reviewed journal

__X__ Accepted by a peer reviewed journal

_____ Published in a Peer reviewed journal

The purpose of this manuscript is to present observations and results of moment of Fe-Mn films obtained with a mapping capability of beamline. The XAS and XMCD of Fe edge was tracked as a sample with gradient of concentration across a critical stoichiometry was prepared. The sudden drop of magnetic moment was followed across physical dimensions of the sample as a grid. The mapping shows the transition from magnetic state to non-magnetic with a greater resolution than seen before.

Abstract

The alloy composition and elemental magnetic moments of bcc single crystal films of compositionally graded Fe_xMn_{1-x} films (20 nm thick films with $0.9 \leq x \leq 0.8$) grown on MgO(001) are spatially mapped using X-ray absorption spectroscopy and magnetic circular dichroism. Electron diffraction measurements on single composition samples confirmed that the structure of Fe_xMn_{1-x} films remained epitaxial and in the bcc phase up to $x = 0.65$, but rotated 45° with respect to the MgO(001) surface net. This is beyond the bulk bcc stability limit of $x = 0.88$. The Fe moment is found to gradually reduce with increasing Mn content with a very abrupt decline at $x = 0.85$, a slightly higher composition than observed in the bulk. Surprisingly, the Mn exhibits a very small net moment ($< 0.1\ \mu_B$) at all compositions, suggesting a complicated Mn spin structure.

Introduction

The bulk Fe_xMn_{1-x} alloy is intriguing because of its departure from the Slater-Pauling curve. Whereas most alloys follow the simple electron-filling model for the entire composition range, the average FeMn alloy moment does so only for the high Fe concentrations[1, 2]. The early bulk studies show that at ~12% Mn concentration (88% Fe), the moment rapidly vanishes, suggesting the onset of a phase transition[2,3]. At low concentrations, the Mn moment was determined by neutron scattering to be small[4-6] or zero[7].

Later theoretical studies using various calculation schemes have examined the bcc Fe_xMn_{1-x} system [8-16] and found general agreement that the Fe moment is found to be mostly constant for high Fe compositions with values ranging from 2.0-2.7 μ_B. Little agreement is present for the Mn moment where it was found to range from being anti-aligned to the Fe moment with a values of 2.4 μ_B (3% Mn)[10], to aligned with the Fe moment with a value of 1.6 μ_B[16] (see ref. 6 for more information).

Single crystal thin films of α-Fe_xMn_{1-x} alloys have been synthesized as thin superlattices with Ir[17,18], on GaAs(001)[19], and on Ag(001)[20]. Deposition on GaAs(001) was found to extend the region of bcc stability to 20% Mn while maintaining ferromagnetism as evidenced by magneto-optic Kerr loops. For these bcc thin films, no direct measure of the Mn moment nor any detailed studies of the onset of ferromagnetism have been reported.

Experimental

To investigate these issues and to examine whether ultrathin films behave similarly to the bulk, 20 nm single crystal Fe_xMn_{1-x} thin film alloys were grown by molecular beam epitaxy (MBE) on polished MgO(001) substrates. The substrates were cleaned using acetone and methanol followed by an *in-situ* vacuum heat cleaning at 800°C. Flux rates were monitored using a quadrupole mass analyzer during growth and subsequently calibrated using Rutherford backscattering spectroscopy. Film crystallinity was monitored using RHEED. Films were terminated with a 3.5-5 nm Al capping layer. Film composition and the elemental moments of the Fe and Mn were independently monitored by X-ray absorption spectroscopy (XAS) and X-ray magnetic circular dichroism (MCD) acquired by sample drain current at Beamline 6.3.1 of the Advanced Light Source.

Two types of samples were synthesized. Primarily, single composition, 20 nm Fe_xMn_{1-x} thin films were grown by co-deposition from separate Fe and Mn sources across the composition range ($0 \leq x \leq 0.7$). Composition was determined from the ratio of the X-ray absorption intensities of the Fe and Mn L_3-edge that was subsequently calibrated by Rutherford Backscattering measurements. The average Fe atomic moment was then determined from the L_3-edge MCD spectra at each composition for comparison with the bulk behavior as determined by Gumlich[2]. (Details of the film growth, structural characterization, and evolution of electronic structure are reported elsewhere.)

The second sample type was a ~20 nm alloy film with a compositional gradient ($0.8 \leq x \leq 0.9$) across the sample accomplished by a slight misalignment of the MBE flux

lobe of the Mn Knudsen cell. RHEED measurements confirmed that the growth of $Fe_{1-x}Mn_x$ films remained epitaxial and in the bcc phase down to x = 0.65 but, like Fe growth[21], is rotated 45° with respect to the MgO(001) surface net. This extends the range of stability for, the bcc structure beyond the bulk bcc stability limit of x = 0.88[22] or x = 0.8 for thin films grown on GaAs(001)[19].

This combinatorial approach is slightly different than the typical combinatorial approach of automated sample production where each sample is compositionally distinct but uniform, generating films suitable for characterization techniques that require separate samples. In this compositional wedge approach, better control of composition, thickness, and interfacial effects can be achieved. Because both the elemental composition and elemental moment are measured using X-ray spectroscopy (XAS and MCD), techniques with very small spatial probes, a single compositional wedge can be used.

The spatial variation of the composition and the magnetic moments was determined using a spatial mapping of the Fe and Mn XAS and MCD L_3-edge intensities with 100 μm by 100 μm spatial resolution (the photon spot size is smaller) accomplished by raster scanning the sample position across the 2.5 mm by 4.5 mm sample. The resulting 4500 scans (1125 positions for 2 elements each requiring an XAS scan using linear polarization with no magnetic field and an MCD scan using circular polarization with ±50 mT field applied in the direction of propagation of the circular polarized photon) can be acquired in a reasonable time due to the new fast scanning capability available at Beamline 6.3.1 of the Advanced Light Source. Full L_{23}-edge scans can be

acquired in a matter of seconds and the entire mapping can be completed in less than a day. Similarly, by automating the analysis procedure, a compositional and elemental moment mapping can be completed in a reasonable time.

The automated analysis for the composition determination consists of a linear background removal of the pre-L_3-edge region and either an integration of the XAS intensity over a defined energy region that includes the entire L_3 peak or a polynomial fit to just the L_3-peak region to establish the XAS peak intensity (and energy position). This is done for both the Fe and Mn L_3-edge. These elemental intensities can be used to create a spatial mapping of the alloy compositions. To validate the XAS analysis process for each scan, the raw data spectrum, the background-subtracted spectrum, and the polynomial-fit superimposed over the data are separately displayed for operator approval prior to inclusion into the compositional mapping.

For the magnetic moment determination, a similar process is used. The MCD spectra are acquired by reversing the applied field at each photon energy for a fixed circular polarization. These intertwined scans are first separated into the individual magnetization scans (+50 mT and -50 mT) followed by a linear background removal of the pre-L_3-edge region of each. The sum and difference spectra are determined and a polynomial fit to just the L_3-peak region of the summed spectrum is used to establish the XAS normalization factor. The difference spectrum is normalized to the incidence angle, degree of circular polarization, and the XAS normalization factor to establish the MCD spectrum. This is followed by either an integration of the MCD intensity over a defined energy region that includes the entire L_3 peak or a polynomial fit to just the L_3-peak

region to establish the MCD peak intensity (and energy position). This is again done for both the Fe and Mn L_3-edge.

These elemental intensities can be used to establish the variation in the elemental moments. To validate the analysis process for each scan, two magnetization separated raw data spectra, both background-subtracted spectra, the summed and difference spectra, the polynomial-fit superimposed over the summed data, and the MCD L_3 area integration or polynomial-fit superimposed over the MCD data are separately displayed for operator approval prior to inclusion into the magnetic moment mapping.

Results and Discussions

Both magnetometry and MCD measurements show that the net magnetic moment of these alloy films behave similarly to the bulk behavior [3]. Figure 1 shows qualitative agreement between the bulk behavior (open circles) and the thin film behavior (filled triangles), the inset will be explained below. It is important to note that the bulk data is the average moment per atom independent of atom type whereas the thin film data is the moment per Fe atom, so a direct quantitative comparison of moment values is not appropriate. The thin film data displays a gradual reduction in the average Fe moment with composition followed by an abrupt decrease at $x = 0.85$ which looks to be much more abrupt than the bulk data reduction. Surprisingly, the Mn moment shows only a very small *net* moment ($< 0.1\ \mu_B$) at all compositions. Varying the deposition conditions (substrate temperature, total flux rate, shuttered Mn evaporator for delta doping, growth

in an applied field) did not increase the observed Mn dichroism signal even for Mn concentrations of 1-2%.

By generating a compositional variation around this critical concentration and subsequently using spatially resolved mapping of the local composition and elemental moments, the moment variation with composition can be determined with high accuracy. Figure 5-2 displays the result of a compositional (left in yellow) and Fe moment (right in red) mapping. The left color scale identifies the small compositional variation (from $0.8 \leq x \leq 0.9$) of this sample and shows one corner of the sample. Composition values for measurements made off the sample were arbitrarily set to zero. For clarity, a compositional contour map is added showing lines of equal composition. Each pixel is 100 μm x 100 μm and the data arrays have been smoothed by averaging over a weighted 3x3 pixel array which replaces the center pixel to improve the image quality. The composition gradually becomes more Mn rich to the right, consistent with the offset of the Mn source to that side of the sample. The apparent composition variation at the left (at 0.4 mm) and top (at 3.8 mm) edges is an artifact created by this averaging and should be ignored.

The Fe moment mapping displays the Fe L_3-edge MCD intensities. Moment values for measurements made off the sample were arbitrarily set to zero. The right color scale shows the MCD intensity arbitrarily normalized to 1. Superimposed on the moment mapping is the composition contour plot, showing that the moment is rather uniform but drops rapidly near the $x \sim 0.85$ composition. Again, the apparent moment reduction at the left and top edges is an artifact of the averaging.

By tabulating the Fe MCD intensity and composition at each recorded position (excluding the sample edge regions) an extremely dense Fe moment vs. composition plot can be obtained. This is shown in the INSET of Figure 5-1 and represents over 300 distinct compositions. The ferromagnetism of the Fe moment is seen to begin a rapid

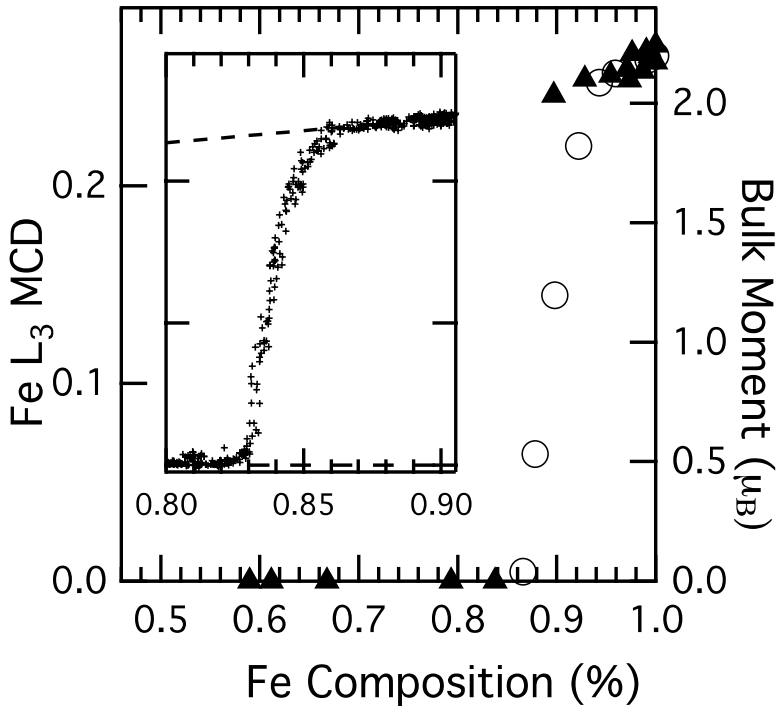

Figure 5-1 : Average atomic moment for bulk FeMn alloy (open circles, right axis) and Fe L3-edge MCD peak intensity for 20 nm FeMn film (filled triangles, left axis) as a function of composition. INSET: Data extracted from moment mapping (see text).

onset at x = 0.83 and is completely established by x = 0.86.

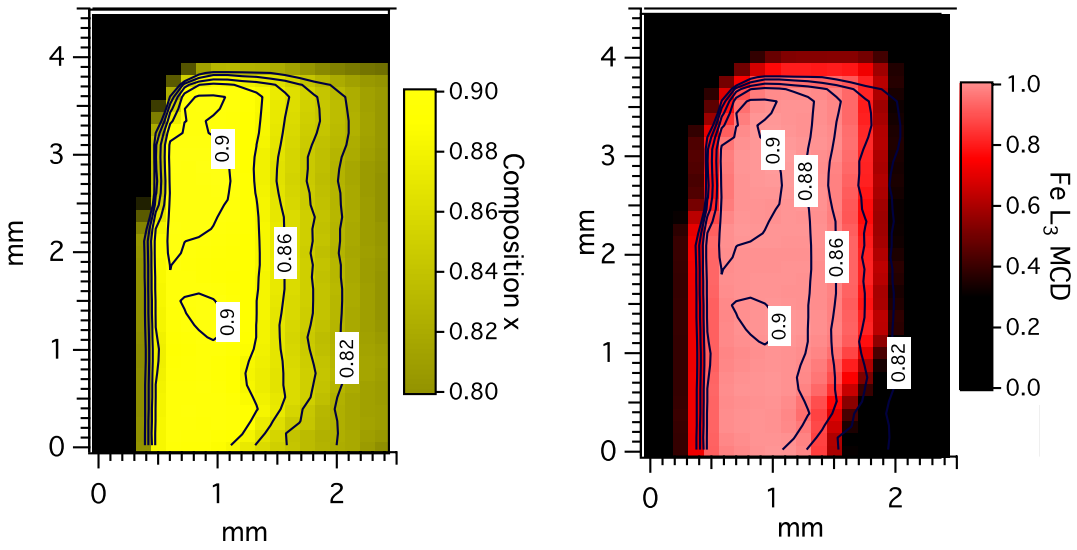

Figure 5-2 LEFT: Compositional map (with color scale and composition contour lines) of a single compositionally graded FexMn1-x sample from $0.8 \leq x \leq 0.9$. RIGHT: Normalized Fe L3-edge MCD intensity map (with color scale) with compositional contour map overlay.

Conclusions

The growth of 20 nm thick bcc Fe_xMn_{1-x} thin films is psuedomorphic to the MgO (001) surface with a 45° rotation up to 35% Mn (x = 0.65), well beyond the bulk stability limit and for films grown on GaAs(001). The variation in the compositional limits of thin film stability suggest that interfacial energies play a major role in stabilization suggesting at these high concentrations the films are not true metastable films but are forced structures similar to the current understanding of bcc Co films[22]. The Fe moment is found to gradually reduce with increasing Mn content with a very abrupt decline at x = 0.85, a slightly higher composition than observed in the bulk. No ferromagnetism is observed at x = 0.80, inconsistent with the Kerr loop hysteresis observations for α-FeMn

on GaAs(001)[19]. Surprisingly, the Mn exhibits a very small net moment (< 0.1 μ_B) at all compositions. This may be due to a small Mn atomic moment[7,14], thermal fluctuations which result in a small averaged atomic moment, or a complex Mn spin structure resulting in no net Mn dichroism signal[11].

To explore this rapid moment reduction, a compositionally graded sample (x = 0.8 to x = 0.9) was spatially mapped for the composition and Fe magnetic moment. Due to advances in data acquisition and analysis, 7200 scans could be processed to generate a compositional and moment map. From this data set, the ferromagnetism of the Fe moment is seen to begin a rapid onset at x = 0.83 (17% Mn) and is completely established by x = 0.86(14% Mn). This range of compositions is most likely due to the limited spatial resolution of the mapping and a higher spatial sampling or a more gradual composition variation may result in a more abrupt transition.

Acknowledgements

The Advanced Light Source is supported by the U.S. Department of Energy under Contract No. DE-AC02-05CH11231. One of us (HB) would like to thank Adam McClure for useful discussions.

References

1. R. M. Bozorth, Ferromagnetism. (IEEE Press, New York, 1951).

2. E. Gumlich, Wiss. Abhandl. Physik-tech. Reichsanstalt. 4, 267-410.

3. H. Yamauchi, H. Watanabe, Y. Suzuki and H. Saito, Journal of the Physical Society of Japan 36 (4), 971-974 (1974).

4. P. Radhakrishna and F. Livet, Solid State Communications 25 (8), 597-600 (1978).

5. F. Kajzar and G. Parette, Physical Review B 22 (11), 5471-5481 (1980).

6. H. R. Child and G. D. Cable, Phys. Rev. B 13, 227 (1976).

7. M. F. Collins and G. G. Low, J. Phys. 25, 596 (1964).

8. E. Ucgun and H. Y. Ocak, Cent. Eur. J. Phys. 6 (4), 808-811 (2008).

9. G. Rahman, I. G. Kim, H. Bhadeshia and A. J. Freeman, Physical Review B 81 (18), 11 (2010).

10. N. I. Medvedeva, D. Van Aken and J. E. Medvedeva, Journal of Physics-Condensed Matter 22 (31) (2010).

11. A. A. Mirzoev, M. M. Yalalov and D. A. Mirzaev, Physics of Metals and Metallography 101 (4), 341-348 (2006).

12. N. I. Kulikov and C. Demangeat, Physical Review B 55 (6), 3533-3542 (1997).

13. D. Music, T. Takahashi, L. Vitos, C. Asker, I. A. Abrikosov and J. M. Schneider, Applied Physics Letters 91 (19) (2007).

14. S. Ghosh, B. Sanyal, C. B. Chaudhuri and A. Mookerjee, European Physical Journal B23 (4), 455-461 (2001).

15. V. I. Anisimov, V. P. Antropov, A. I. Liechtenstein, V. A. Gubanov and A. V. Postnikov, Physical Review B 37 (10), 5598-5602 (1988).

16. C. Koenig and E. Daniel, J. Phys. (Paris) 42, 1015 (1981).

17. H. Fischer, S. Andrieu, P. Bauer and M. Piecuch, Mat. Res. Soc. Symp. Proc. 364,

271 (1995).

18. A. Dechelette, J. M. Tonnerre, M. C. Saint Lager, F. Bartolome, L. Seve, D. Raoux, H. Fischer, M. Piecuch, V. Chakarian and C. C. Kao, Physical Review B 60 (9), 6636-6645 (1999).

19. C. Jing, Y. Z. Wu, Z. X. Yang, G. S. Dong and X. F. Jin, J. Magn. Magn. Mater. 198- 99, 270-272 (1999).

20. R. Paniago, J. L. Lopez and H. D. Pfannes, Ultra-thin FexMn1-x alloy films on Ag(100). (2002).

21. A. McClure, E. Arenholz and Y. U. Idzerda, J. Vac. Sci. Tech. A 28, 969 (2010).

22. A. Y. Liu and D. J. Singh, Journal of Applied Physics 73 (10), 6189-6191 (1993).

CHAPTER SIX

DISCUSSION AND CONCLUSION

The Complex Problem of Fe-Mn

The main aspect of the Fe-Mn system is that it has demonstrated contrasting results regarding magnetic moment of manganese and also the coupling to the Iron surroundings. To give you a perspective of what this issue is I have described a few examples of the Fe-Mn findings either from experiments or from theoretical calculations.

To try to understand Fe-Mn system one approach is to start with pure Fe and Mn crystal structures and their magnetic characters. Just that itself gives us the idea of what combinations are possible in nature.

Firstly, it is known that from, well studied, phase diagrams of Fe that Fe exists in fcc and bcc form. The fcc Fe has been shown to have AFM and NM as two of almost degenerate ground states favoring over FM. Yet, fcc Fe can exist in either low spin or high spin FM order in some theories.[1]

For Mn, it also has been shown to exist in fcc and infrequently, in bcc structure for small portion of phase space before settling into its complex unit cell alpha structure or A12 structure for large part of phase diagram. The fcc Mn structure may be why it can form a stable gamma-Fe-Mn structure which has lent its exchange bias properties as a pinning AFM layer in spin valve devices.

The fcc and bcc Mn structures both have been predicted to have AFM and NM ground state from calculations of Moruzzi and Kubler[1].

Experiments done with neutron scattering can distinguish elemental magnetic moments of Fe and Mn. The findings from 5 to 9% Mn in bcc FeMn have shown that Mn has very low (0.7 +-0.25 Bohr magneton) moment at low temperature, and Fe has 2.23+-0.01 Bohr magneton moment. They have noted that, many calculations overestimate the Mn moment than the neutron scattering data [2]. Theoretical calculations of Shirley et.al. predict Mn moment to be 1.5 Bohr magneton. There after neutron scattering experimental data of Collins and Low showed Mn had moment of barely 0.2 Bohr magneton.

One explanation of the variation of magnetic order in fcc Fe-Mn may be that, magnetovolume effects play a role in determining net contribution from each unit cell of the crystal. In such materials, the volumetric separation due to atomic sizes or any other factor determine the sign and the magnitude of the magnetic moment. If the fcc Fe Mn film is on a substrate which is smaller than the film there is AFM coupling seen in the Fe-Mn film. The film is compressed when it is deposited, as it grows, the volume is relatively smaller than the relaxed case. Such a system has been found by theoretical calculations to be NM state, also seen in experiments. If the substrate is larger, however, the magnetic interaction results in an AFM state.[1]

Discussion

Let us consider the summary of the results for discussion. As partly seen and explained in the first manuscript, we note some interesting features in the XAS of Fe and Mn. We observe, in the figure 4 of chapter 4 that, the L_3 peak of Fe shifts a bit to higher energy as we increase the concentration of Mn. How do we explain this behavior? First

of all, let us remind ourselves what Peak really means in terms of electronic transitions. It represents a very large number of transitions from p state to unfilled d state near (just above) the Fermi level.

The energy difference between the core state p and the lowest unfilled d state is called the binding energy. If the Fermi level is also where the maximum number of available states is, then the peak basically rides right on top of the Fermi level. So, if the Fermi level moves up due to alloying, then the maximum number of transitions will be altered according to the shape of the density of states above the original Fermi level. The difference between the energy at maximum number of transitions and the core state is now increased because Fermi level has increased. This results in the energy increase in the Fe XAS as the Mn starts to fill the bands. The XAS spectra are L_3 peak height normalized, rather than area-normalized as is the case usually with the oxides.

Yet we do not detect any corresponding peak position shift to higher or lower energy for Mn XAS. This means that, the maximum possible number of transitions is not affected by the change in Fermi level. This can be explained similarly based on position of Fermi level with respect to where the maximum of unoccupied states is in the Mn band structure. If the Fermi level already starts slightly below the peak, then we can see that, the peak of the spectrum is insensitive to the small changes in Fermi level as peak stays above the changes. This also brings out the feature that the binding energy may be defined where the slope of the rising edge changes sign, a point of inflection.

The shoulder feature of MCD of Fe indicates that Mn is alloying rather than just remaining as a cluster.

As we increase the concentration of Mn, one should expect the moment of Fe and Mn should track the change. We see that moment of Fe only tracks the change in concentration as a shift in energy. The Mn L_3 peak shows no such tracking.

The MCD of Fe shows usual magnetic moment and it also shows a trend to decrease in magnitude as shown in the inset superposed on bulk data from Gumlich [source]. As in the conventional Slater Pauling curve, the Gumlich data shows linear decrease in the bulk moment and then a sudden collapse from 12% onwards. The Fe moment also shows decrease but at a lower slope. In the previous work, Gumlich data shows average moment of bulk. If the behavior of Fe moment per unit atom versus concentration of Mn is adjusted for the dilution effect, then the two slopes can be reconciled.

Moment of Mn is a curious case. The low moment can be due to two processes; Fe-Mn interaction and Mn-Mn interaction. In the high concentration of Mn, the Mn-Mn interaction can be thought to dominate as there may be a neighboring Mn atom near enough to align with. That should have given a significant moment in alloys. But this has not been observed; rather only a weak ferromagnetic signature is seen on the Mn. The MCD spectrum on Mn shows a derivative like shape at the L_3 edge. The nature of this shape is usually associated with how the density of states is shaped with respect to the spins. Second peak is a typical shape for metallic material. To evaluate the reasons, allow ourselves to image the bcc structure of Fe and bcc Mn cubes interlocked with each other. As the moments at each vertex of the cube of Fe should be aligned according to our MCD information, we have ferromagnetic Fe lattice. As for the Mn structure, if the alignment

of the moment was along any biaxial direction, we would have seen much larger moment in MCD of Mn. We do not see any significant moment in Mn MCD. This could happen, if the Mn vertices over the cube or parts of the cube, did not align bi-axially, but rather had non-collinear arrangement. This would result in a very low net moment in Mn sub structure. Also, the type of observed coupling between the small moment of Mn and large moment of Fe is FM as confirmed by the same sign of the MCDs of Mn and Fe.

To see that the moment of Mn could be changed if the Mn-Fe interaction changes its magnitude, we bring down the Mn concentration to very small value. This was tried with couple of ways. One was to grow samples at low substrate temperature to lock the incoming beam of Mn atoms in position avoiding any clustering by rearrangement. Secondly, to ensure the Fe and Mn atoms are well intermixed, and Mn atoms stay far away from its next Mn atom, I tried Atomic Beam epitaxy method or delta-doping. In this method essentially, I exposed the substrate alternately to Fe and Mn sources. That makes sure that the concentration of Mn is low and the distribution of the Mn is sparse enough to assume no clustering. Yet, there is small and unchanged moment in Mn. This case is also very interesting. Pairwise exchange interactions between neighboring Mn and Fe atoms need to be considered carefully. The geometry of the structure with Fe atoms on the vertices of cube of the fcc or our case, bcc, with Mn lattice either in the body center or at a vertex should be visualized. The direction of magnetic moment at the Mn atom will be selected by configuration that gives the lowest energy for the spin arrangement and for the atomic configuration. The collinear arrangements, that is aligned or anti aligned cannot explain the small definite moment of Mn. It should give a strong moment

either parallel or antiparallel to the Fe lattice. Thus one must think of non-collinear exchange interactions. This has been able to explain a lot of AFM structures which show small FM signal in low concentrations. To explain, let us look at the Dzyaloshinskii Moriya (DM) interaction [3,4]. The coupling between neighboring spins depends on the energy between two spins, which contains isotropic exchange term, exchange anisotropy and an antisymmetric exchange term. The last term basically inverts (reverses) the spins and positions, is called DM vector, **D** usually included in the interaction energy expression as follows.

$$\Delta E = \sum_{m \neq n} J_{mn} S_m \cdot S_n + \sum_{m \neq n} D_{mn} \cdot [S_m \times S_n] - \mu_B g S \sum_m H \cdot S_m$$

Summation runs over all magnetic atoms. The $\mathbf{D_{mn}}$ vectors depend on the relative positions of the magnetic atoms. J_{mn} are the exchange coefficients which can select either parallel or antiparallel coupling. S_m is a unit vector in the direction of the m^{th} spin of magnitude S. Gyromagnetic ratio is g (about 2) and Bohr magneton has the usual meaning.

Inspecting above equation, we can see that if the first term dominates, then the coupling is collinear giving parallel or antiparallel magnetic order in the whole structure. If the second term dominates, the alignment of magnetic moment is orthogonal.

The interplay between these terms basically, can explain weak ferromagnetism in unusual spins geometries of certain AFM structures. [5]

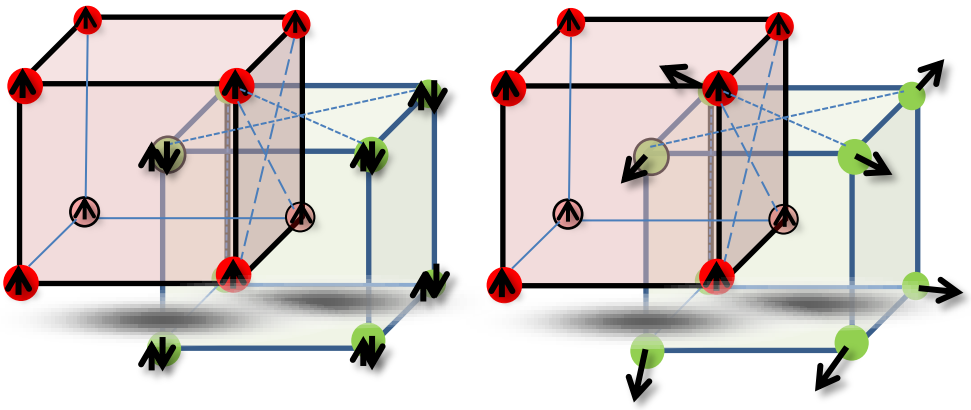

Figure 6-1 left: Collinear Moment arrangement, right: non-collinear arrangements. Red circles represent Fe atoms, Green circles represent Mn

Conclusions

In closing, we have been able to make bcc MnFe single crystal thin film on MgO(001) substrate. The structural stability has been seen up to 35% of Mn concentration. The magnetic order can be seen to collapse only for Fe and it occurs very sharply within 3% around 85 % Fe concentration. The Mn moment, obtained by x-ray spectroscopy techniques, is seen to be very small and is aligned ferromagnetically with the Fe moment. The Fe behavior is consistent with the bulk behavior even in the thin film form in bcc. The Mn moment behavior is matter of further investigation. For low concentration of Mn, the observed weak FM moment could be due to non-collinear exchange interactions thus explaining part of the Slater Pauling behavior of FeMn system.

Future Directions

The work can be extended into more combinations of binary or ternary systems which could be of interest as exchange bias materials for applications in memory devices. One such binary system of interest is Co-Mn, has recently been made in the MBE system just prior to writing up this work on FeMn. Though the primary results are being analyzed, the MBE system can be used to make more such materials. The analysis of data acquired in the XAS mapping can be huge and one needs to work on a computer code that can spew out the maps from the data without human oversight. A possible automation in data analysis could help to rapidly generate mapping of moment. The exciting non-collinear magnetic moment materials including oxides could be looked into for further work. In-situ RHEED imaging as the thickness is increasing could be investigated for checking if there is thickness dependence to the magnetic or structural order. A model that includes fcc and bcc phases could be simulated for seeing any mixing of phase effects. A set of samples with uniform concentration near 15% Mn concentration could be measured to decrease any contribution from other concentrations as could be present in a gradient sample. All in all, it opens a lot of possibilities for future.

References

1. Moruzzi, V.L., P.M. Marcus, and J. Kübler, Magnetovolume instabilities and ferromagnetism versus antiferromagnetism in bulk fcc iron and manganese. Physical Review B, 1989. 39(10): p. 6957-6961.

2. Nakai, Y. and N. Kunitomi, Magnetic-Moment Distribution in Bcc Fe-Mn Alloys. Journal of the Physical Society of Japan, 1975. 39(5): p. 1257-1262.

3. Moriya, T., Anisotropic Superexchange Interaction and Weak Ferromagnetism. Physical Review, 1960. 120(1): p. 91-98.

4. Dzyaloshinsky, I., A thermodynamic theory of "weak" ferromagnetism of antiferromagnetics. Journal of Physics and Chemistry of Solids, 1958. 4(4): p. 241-255.

5. Dmitrienko, V.E., et al., Measuring the Dzyaloshinskii-Moriya interaction in a weak ferromagnet. Nat Phys, 2014. 10(3): p. 202-206.

REFERENCES CITED

1. Anisimov, V.I., et al., ELECTRONIC-STRUCTURE AND MAGNETIC-PROPERTIES OF 3D IMPURITIES IN FERROMAGNETIC METALS. Physical Review B, 1988. 37(10): p. 5598-5602.

2. Ashcroft, N.W. and N.D. Mermin, Solid state physics. 1976, New York,: Holt. xxi, 826 p.

3. Bagayoko, D. and J. Callaway, LATTICE-PARAMETER DEPENDENCE OF FERROMAGNETISM IN BCC AND FCC IRON. Physical Review B, 1983. 28(10): p. 5419-5422.

4. Baibich, M., et al., Giant Magnetoresistance of (001)Fe/(001)Cr Magnetic Superlattices. Physical Review Letters, 1988. 61(21): p. 2472-2475.

5. Berkowitz, A.E. and K. Takano, Exchange anisotropy - a review. Journal of Magnetism and Magnetic Materials, 1999. 200(1-3): p. 552-570.

6. Boubeta, C.M., J.L. Costa-Kramer, and A. Cebollada, Epitaxy, magnetic and tunnel properties of transition metal/MgO(001) heterostructures. Journal of Physics-Condensed Matter, 2003. 15(25): p. R1123-R1167.

7. Bowen, M., et al., Large magnetoresistance in Fe/MgO/FeCo(001) epitaxial tunnel junctions on GaAs(001). Applied Physics Letters, 2001. 79(11): p. 1655-1657.

8. Bradley, A.J. and J. Thewlis, The crystal structure of alpha-manganese. Proceedings of the Royal Society of London Series a-Containing Papers of a Mathematical and Physical Character, 1927. 115(771): p. 456-471.

9. Bunker, G., Introduction to XAFS : a practical guide to X-ray absorption fine structure spectroscopy. 2010, Cambridge, UK ; New York: Cambridge University Press. viii, 260 p.

10. Buschow, K.H.J. and F.R.d. Boer, Physics of magnetism and magnetic materials. 2003, New York: Kluwer Academic/Plenum Publishers. vii, 182 p.

11. Bozorth, R.M., Atomic Moments of Ferromagnetic Alloys. Physical Review, 1950. 79(5): p. 887-887.

12. Child, H. and J. Cable, Temperature dependence of the magnetic-moment distribution around impurities in iron. Physical Review B, 1976. 13(1): p. 227.

13. Collins, M.F. and G.G. Low, Magnetic Moment Distribution around Transition Element Impurities in Iron and Nickel. Proceedings of the Physical Society of London, 1965. 86(551P): p. 535-&.

14. Déchelette, A., et al., Magnetic properties of bct Fe_{x}Mn_{1-x} thin-film alloys investigated by linearly polarized soft-x-ray resonant magnetic reflectivity. Physical Review B, 1999. 60(9): p. 6636-6645.

15. DeGroot, F. and A. Kotani, Core Level Spectroscopy of Solids. Core Level Spectroscopy of Solids, 2008. 6: p. 1-490.

16. Dmitrienko, V.E., et al., Measuring the Dzyaloshinskii-Moriya interaction in a weak ferromagnet. Nat Phys, 2014. 10(3): p. 202-206.

17. Dresselhaus, J., et al., Antiferromagnetic coupling of Mn adsorbates to Fe(100). Physical Review B, 1997. 56(9): p. 5461-5467.

18. Dresselhaus, J., et al., Probing the magnetism of MnFe surface alloys on Fe(100) by circular magnetic dichroism and total yield microscopy. Surface Science, 1997. 377(1-3): p. 450-456.

19. Drittler, B., et al., ELECTRONIC-STRUCTURE AND MAGNETIC-PROPERTIES OF DILUTE FE ALLOYS WITH TRANSITION-METAL IMPURITIES. Physical Review B, 1989. 40(12): p. 8203-8212.

20. Dzyaloshinsky, I., A thermodynamic theory of "weak" ferromagnetism of antiferromagnetics. Journal of Physics and Chemistry of Solids, 1958. 4(4): p. 241-255.

21. Eisberg, R.M. and R. Resnick, Quantum physics of atoms, molecules, solids, nuclei, and particles. 2nd ed. 1985, New York: Wiley.

22. Elzain, M.E. and A.A. Yousif, ELECTRONIC AND MAGNETIC-STRUCTURE OF BCC FE-MN ALLOYS. Physica Status Solidi B-Basic Research, 1993. 178(2): p. 451-458.

23. Endoh, Y. and Y. Ishikawa, Antiferromagnetism of γ Iron Manganes Alloys. Journal of The Physical Society of Japan, 1971. 30(6): p. 1614-1627.

24. Endoh, Y. and Y. Ishikawa, ANTIFERROMAGNETISM OF GAMMA IRON MANGANES ALLOYS. Journal of the Physical Society of Japan, 1971. 30(6): p. 1614-&.

25. Finkel, V.A., Crystal Structure of Manganese between 77 Degrees K and 300 Degrees K. Soviet Physics Jetp-Ussr, 1968. 27(6): p. 910-&.

26. Fuster, G., et al., MAGNETISM IN BCC AND FCC MANGANESE. Physical Review B, 1988. 38(1): p. 423-432.

27. Hafner, J. and D. Hobbs, Understanding the complex metallic element Mn. II. Geometric frustration in beta-Mn, phase stability, and phase transitions. Physical Review B, 2003. 68(1).

28. Hasegawa, H. and D.G. Pettifor, Microscopic Theory of the Temperature-Pressure Phase-Diagram of Iron. Physical Review Letters, 1983. 50(2): p. 130-133.

29. Herman, M.A. and H. Sitter, Molecular beam epitaxy : fundamentals and current status. 2nd, rev. and updated ed. Springer series in materials science. 1996, Berlin ; New York: Springer. xiv, 453 p.

30. Hobbs, D., J. Hafner, and D. Spisak, Understanding the complex metallic element Mn. I. Crystalline and noncollinear magnetic structure of alpha-Mn. Physical Review B, 2003. 68(1).

31. Jaccarino, V., L.R. Walker, and G.K. Wertheim, LOCALIZED MOMENTS OF MANGANESE IMPURITIES IN FERROMAGNETIC IRON. Physical Review Letters, 1964. 13(25): p. 752-&.

32. Jonker, B.T., G.A. Prinz, and Y.U. Idzerda, Interface Formation and Film Morphology for Growth of Fe and Co on Znse(001). Journal of Vacuum Science & Technology B, 1991. 9(4): p. 2437-2444.

33. Jungblut, R., et al., Orientational Dependence of the Exchange Biasing in Molecular-Beam-Epitaxy-Grown Ni80fe20/Fe50mn50 Bilayers. Journal of Applied Physics, 1994. 75(10): p. 6659-6664.

34. Kajzar, F. and G. Parette, Magnetic-moment distribution and environmental effects in dilute iron-based alloy with V, Cr, and Mn impurities. Physical Review B, 1980. 22(11): p. 5471.

35. Kanaji, T., T. Kagotani, and S. Nagata, Auger and Loss Spectroscopy Study of Surface Contamination Effect on Growth Mode of Iron Epitaxial-Films on Mgo(001). Thin Solid Films, 1976. 32(2): p. 217-219.

36. Kang, S.G., et al., MOSSBAUER-EFFECT STUDY OF BCC FE-MN ALLOYS. Journal of the Physical Society of Japan, 1974. 36(4): p. 975-979.

37. Kasuya, T., A Theory of Metallic Ferro- and Antiferromagnetism on Zener's Model. Progress of Theoretical Physics, 1956. 16(1): p. 45-57.

38. Kittel, C., Introduction to solid state physics. 8th ed. 2005, Hoboken, NJ: Wiley. xix, 680 p.

39. Litvinov, V., et al., Electron Redistribution and the Stability of the Body-Centered Cubic Structure in Iron--Manganese Alloys. Fiz. Met. Metalloved., 1979. 47(1): p. 96-101.

40. Liu, Y., D. Shindō, and D.J. Sellmyer, Handbook of advanced magnetic materials. 2006, New York Beijing: Springer ;Tsinghua University Press.

41. Mayer, M., SIMNRA, a simulation program for the analysis of NRA, RBS and ERDA. Application of Accelerators in Research and Industry, Pts 1 and 2, 1999. 475: p. 541-544.

42. Medvedeva, N.I., D. Van Aken, and J.E. Medvedeva, Magnetism in bcc and fcc Fe with carbon and manganese. Journal of Physics-Condensed Matter, 2010. 22(31): p. 7.

43. Meng, K.K., et al., Magnetic properties of Fe0.4Mn0.6/Co2FeAl bilayers grown on GaAs by molecular-beam epitaxy. Journal of Applied Physics, 2011. 110(9).

44. Mirzoev, A.A., D.A. Mirzaev, and M.M. Yalolov, Magnetic State of Components of Fe-Mn Alloys and Mixing energy: First-Principles Calculation. World Congress on Engineering 2009, Vols I and Ii, 2009: p. 130-135.

45. Mirzoev, A.A., M.M. Yalalov, and D.A. Mirzaev, Energy of mixing and magnetic state of components of Fe-Mn alloys: A first-principles calculation for the ground state. Physics of Metals and Metallography, 2006. 101(4): p. 341-348.

46. Moriya, T., Anisotropic Superexchange Interaction and Weak Ferromagnetism. Physical Review, 1960. 120(1): p. 91-98.

47. Moruzzi, V.L., P.M. Marcus, and J. Kubler, Magnetovolume Instabilities and Ferromagnetism Versus Antiferromagnetism in Bulk Fcc Iron and Manganese. Physical Review B, 1989. 39(10): p. 6957-6961.

48. Nakai, Y. and N. Kunitomi, Magnetic-Moment Distribution in Bcc Fe-Mn Alloys. Journal of the Physical Society of Japan, 1975. 39(5): p. 1257-1262.

49. Nogues and I.K. Schuller, Exchange bias. Journal of magnetism and magnetic materials, 1999. 192(2): p. 203-232.

50. Paduani, C. and E.G. daSilva, Electronic structure of disordered alpha-FeMn alloys. Journal of Magnetism and Magnetic Materials, 1996. 161: p. 184-188.

51. Park, J.H., et al., Non-collinear magnetism in itinerant electron systems: Fe, Co, and Ni. Journal of the Korean Physical Society, 2000. 37(2): p. 109-113.

52. Parkin, S.S.P., et al., Giant tunnelling magnetoresistance at room temperature with MgO (100) tunnel barriers. Nature Materials, 2004. 3(12): p. 862-867.

53. Pauling, L., The Nature of the Interatomic Forces in Metals. Physical Review, 1938. 54(11): p. 899-904.

54. Prinz, G.A. and J.J. Krebs, Molecular-Beam Epitaxial-Growth of Single-Crystal Fe Films on Gaas. Applied Physics Letters, 1981. 39(5): p. 397-399.

55. Radhakrishna, P. and F. Livet, ENVIRONMENTAL EFFECTS IN IRON-MANGANESE ALLOYS. Solid State Communications, 1978. 25(8): p. 597-600.

56. Rosenberg, R.A., M.W. Mcdowell, and J.R. Noonan, X-Ray Photoelectron-Spectroscopy Analysis of Aluminum and Copper Cleaning Procedures for the Advanced Photon Source. Journal of Vacuum Science & Technology a-Vacuum Surfaces and Films, 1994. 12(4): p. 1755-1759.

57. Ruderman, M.A. and C. Kittel, Indirect Exchange Coupling of Nuclear Magnetic Moments by Conduction Electrons. Physical Review, 1954. 96(1): p. 99-102.

58. Shull, C. and M. Wilkinson, Neutron Diffraction Studies of Various Transition Elements. Reviews of Modern Physics, 1953. 25(1): p. 100-107.

59. Slater, J.C., Electronic structure of alloys. Journal of Applied Physics, 1937. 8(6): p. 385-390.

60. Stavitski, E. and F.M.F. de Groot, The CTM4XAS program for EELS and XAS spectral shape analysis of transition metal L edges. Micron, 2010. 41(7): p. 687-694.

61. Stöhr, J., NEXAFS spectroscopy. Springer series in surface sciences. 1992, Berlin ; New York: Springer-Verlag. xv, 403 p.

62. Stöhr, J. and H.C. Siegmann, Magnetism : from fundamentals to nanoscale dynamics. Springer series in solid-state sciences,. 2006, Berlin ; New York: Springer. xvii, 820 p.

63. Suss, F. and U. Krey, On the Itinerant Magnetism of Mn and Its Ordered Alloys with Fe and Ni. Journal of Magnetism and Magnetic Materials, 1993. 125(3): p. 351-362.

64. Tsuchiya, Y., et al., Magnetic properties and magnetic phase diagram of bcc Cr-Fe-Mn alloys. Journal of the Physical Society of Japan, 1996. 65(10): p. 3289-3293.

65. Umebayas.H and Y. Ishikawa, Antiferromagnetism of Gamma Fe-Mn Alloys. Journal of the Physical Society of Japan, 1966. 21(7): p. 1281-&.

66. Urano, T. and T. Kanaji, Atomic and Electronic-Structure of Ultrathin Iron Film on Mgo(001) Surface. Journal of the Physical Society of Japan, 1988. 57(10): p. 3403-3410.

67. Williams, A.R., et al., Transition between fundamental magnetic behaviors revealed by generalized Slater–Pauling construction. Journal of Applied Physics, 1984. 55(6): p. 2353.

68. Willis, R.F. and N. Janke-Gilman, Distinguishing magnetic-moment and magnetic-ordering behavior on the Slater-Pauling curve. Europhysics Letters (EPL), 2005. 69(3): p. 411-416.

69. Winick, H., Synchrotron radiation sources : a primer. World Scientific series on synchrotron radiation techniques and applications. 1994, Singapore ; River Edge, N.J.: World Scientific. xix, 507 p.

70. Yamauchi, H., et al., MAGNETIZATION OF ALPHA-PHASE FE-MN ALLOYS. Journal of the Physical Society of Japan, 1974. 36(4): p. 971-974.